

# Stellar orbit evolution in close circumstellar disc encounters

D. J. Muñoz<sup>1,2\*</sup>, K. Kratter<sup>3</sup>, M. Vogelsberger<sup>1</sup>, L. Hernquist<sup>1</sup> and V. Springel<sup>4,5</sup>

<sup>1</sup> *Harvard-Smithsonian Center for Astrophysics, 60 Garden Street, Cambridge, MA 02138, USA*

<sup>2</sup> *Center for Space Research, Department of Astronomy, Cornell University, Ithaca, NY 14853, USA*

<sup>3</sup> *Steward Observatory, University of Arizona, 933 North Cherry Ave, Tucson, AZ, 85721, USA*

<sup>4</sup> *Heidelberg Institute for Theoretical Studies, Schloss-Wolfsbrunnengasse 35, 69118 Heidelberg, Germany*

<sup>5</sup> *Zentrum für Astronomie der Universität Heidelberg, ARI, Mönchhofstr. 12-14, 69120 Heidelberg, Germany*

21 September 2018

## ABSTRACT

The formation and early evolution of circumstellar discs often occurs within dense, newborn stellar clusters. For the first time, we apply the moving-mesh code AREPO, to circumstellar discs in 3-D, focusing on disc-disc interactions that result from stellar fly-bys. Although a small fraction of stars are expected to undergo close approaches, the outcomes of the most violent encounters might leave an imprint on the discs and host stars that will influence both their orbits and their ability to form planets. We first construct well-behaved 3-D models of self-gravitating discs, and then create a suite of numerical experiments of parabolic encounters, exploring the effects of pericenter separation  $r_p$ , disc orientation and disc-star mass ratio ( $M_d/M_*$ ) on the orbital evolution of the host stars. Close encounters ( $2r_p \lesssim$  disc radius) can truncate discs on very short time scales. If discs are massive, close encounters facilitate enough orbital angular momentum extraction to induce stellar capture. We find that for realistic primordial disc masses  $M_d \lesssim 0.1M_*$ , non-colliding encounters induce minor orbital changes, which is consistent with analytic calculations of encounters in the linear regime. The same disc masses produce entirely different results for grazing/colliding encounters. In the latter case, rapidly cooling discs lose orbital energy by radiating away the energy excess of the shock-heated gas, thus causing capture of the host stars into a bound orbit. In rare cases, a tight binary with a circumbinary disc forms as a result of this encounter.

**Key words:** hydrodynamics – methods: numerical – planets and satellites: formation – protoplanetary discs – binaries: general.

## 1 INTRODUCTION

The variety of processes that influence circumstellar disc evolution in multi-star systems are not yet well understood. discs can be influenced by the primordial cluster kinematics, with important consequences for planet formation. In contrast with observations of more evolved Class II objects (for which there is evidence that multiplicity can have a strong influence on disc sizes and morphologies) Class 0 objects are more elusive from direct observation (e.g. Jørgensen et al. 2009; Chen et al. 2013; Chiang, Looney & Tobin 2012; Tobin et al. 2013; Murillo et al. 2013). Nevertheless, the existence of evolved discs in binary systems implies that earlier, massive rotating structures must have interacted in some way with stars other than their host. Exploring these more violent interactions, where pericenter separation becomes comparable to disc size, requires high resolution, three dimensional numerical simulations.

The role of stellar flybys in planet formation has been explored from the point of view of planet stability (e.g. Adams & Laughlin 2001; Adams et al. 2006; Dukes & Krumholz 2012) through exhaustive Monte Carlo  $N$ -body methods. The detailed effects of stellar flybys on single gas discs have also been explored through

isolated simulations (e.g. Forgan & Rice 2009; Sheppard & Trujillo 2006; Moeckel & Bally 2006; Shen et al. 2010; Thies et al. 2010). Close passages can truncate discs, which affects planet formation, and also trigger gravitational instabilities in discs (e.g. Shen et al. 2010; Thies et al. 2010). Nearby stars also accelerate disc photo-evaporation even when their dynamical influence is small (Anderson, Adams & Calvet 2013).

Bound multiple systems affect disc evolution and planet formation radically. The perturbations from a stellar-mass companion lead to tidal truncation (e.g., Artymowicz & Lubow 1994), warping/bending (e.g., Larwood et al. 1996; Ogilvie & Dubus 2001) or hastened disc dispersal (e.g., Alexander 2012; Kraus & Ireland 2012; Harris et al. 2012). Recent observations of pre-main sequence stars in binary systems have directly confirmed the importance of some of these effects. disc size has been shown to depend strongly on stellar separation (Harris et al. 2012) and close passages have been associated with major disruptions in disc geometry, although these might require additional physics (e.g. winds, external photo-evaporation) other than the gravitational interactions between the disc and a companion star (see e.g., Cabrit et al. 2006; Salyk et al. 2014).

In principle, the higher order multipole moments of a massive circumstellar disc’s potential could modify stellar encounters. Al-

\* E-mail: dmunoz@astro.cornell.edu

though disc masses of pre-main sequence stars (e.g. Class II young stellar objects) are not expected to exceed 1% of the host star's mass (e.g. Andrews & Williams 2007; Andrews et al. 2009), very early protostellar objects are expected to have more massive discs or envelopes. The role of these massive young discs/envelopes on stellar dynamics has not been explored much theoretically, but it is possible that the gas component plays a short lived, but important role that cannot be captured by simple collisionless dynamics.

Despite the increased sophistication of cluster models (Adams et al. 2006; Parker & Quanz 2012; Bate 2011, 2012; Craig & Krumholz 2013), the dynamical range required on timescales of  $N$ -body systems of stars with respect to their planetary systems makes direct simulation of full clusters prohibitive computationally. Instead, we isolate two-body systems in order to study disc-disc interactions at high resolution.

In this work, we focus on the direct simulation of circumstellar disc flybys, solving the equations of three-dimensional, self-gravitating hydrodynamics discretized over a moving Voronoi mesh as implemented by the AREPO code (Springel 2010a). In Section 2, we describe the numerical set-up, detailing the individual disc models and the orbital configuration of the disc encounters. We summarize the results of the numerical experiments in Section 3, focusing on the evolution of the stellar orbits. In Section 4, we discuss the consequences of these disc encounters and the plausibility and rate of their occurrence.

## 2 NUMERICAL EXPERIMENTS ON DISC-DISC INTERACTION

### 2.1 Previous work

Numerical experiments with isolated configurations of star-disc and disc-disc interaction on spatial scales of  $\sim 100$  AU enable the detailed study of regions that are usually unresolved in self-consistent, *ab initio* simulations of star forming clouds with spatial scales of  $\sim 10^5$  AU. Note that even the state-of-the-art star formation simulations of Bate (2012) – which form discs around protostars – have an SPH particle mass of  $1.43 \times 10^{-5} M_\odot$ , implying that a  $0.01 M_\odot$  disc is composed of barely 700 resolution elements.

Despite the rareness of events like direct star-disc and disc-disc interactions, such encounters have received significant attention in the literature, either focusing on their role in the tidal evolution of a binary and orbital capture (Clarke & Pringle 1991a,b; Ostriker 1994), or by studying the possible triggering of spiral arms, gravitational instability (GI) and fragmentation (Boffin et al. 1998; Lin et al. 1998; Pfalzner 2003; Pfalzner, Umbreit & Henning 2005; Pfalzner & Olczak 2007; Forgan & Rice 2009; Shen et al. 2010).

Studies of disc-disc collisions by direct numerical simulation date back to Lin et al. (1998) and Watkins et al. (1998a,b) (see also Boffin et al. 1998), where authors hypothesized that condensation of material in tidally induced tails could produce a population of brown dwarfs. This idea has been revisited both with pure  $N$ -body approaches (Pfalzner 2003; Pfalzner, Umbreit & Henning 2005; Thies, Kroupa & Theis 2005; Pfalzner & Olczak 2007) and with gas dynamics (Forgan & Rice 2009; Sheppard & Trujillo 2006; Shen et al. 2010; Thies et al. 2010). All the hydrodynamical studies included self-gravity, although some of the  $N$ -body ones used test particles (e.g. Pfalzner, Umbreit & Henning 2005), only focusing on the passive response of the disc to an external perturber. These studies have concentrated on the tidal generation of spiral arms (e.g. Pfalzner 2003); on disc fragmentation and formation of substellar

mass objects (e.g. Lin et al. 1998; Sheppard & Trujillo 2006; Shen et al. 2010; Thies et al. 2010) and disc truncation (e.g. Forgan & Rice 2009) and, more recently, on the stability of disc-embedded planets (Picogna & Marzari 2014). Those studies that include gas were all carried out using smoothed particle hydrodynamics (SPH; Lucy 1977; Gingold & Monaghan 1977; Monaghan 1992; Springel 2010b).

The fact that SPH has been the method of choice for disc-disc interaction reflects the necessity of having a geometrically flexible numerical scheme (e.g., without preferred orientations/symmetries). Isolated discs are nearly axisymmetric, and thus benefit from the use of structured grids in cylindrical coordinates, since such grid configurations favor low numerical diffusivity for azimuthal flow. As soon as this symmetry is broken (e.g., by combining two circumstellar discs moving at supersonic speeds toward each other), the benefit of structured grids becomes less clear. Consequently, this problem is ideal for a quasi-Lagrangian Eulerian code like AREPO (Springel 2010a), in which the control volumes evolve and move in a similar way to SPH particles; i.e., by following the local velocity field. Yet by being locally a grid code, AREPO does not suffer from some of the numerical artifacts SPH is known to develop, such as clumping instabilities, suppression of hydrodynamic instabilities, artificial surface tension, zeroth order error terms, etc (see Vogelsberger et al. 2012; Sijacki et al. 2012; Bauer & Springel 2012; Dehnen & Aly 2012). One of the main advantages of using a code like AREPO for circumstellar disc simulations is the minimization of the so-called “high Mach number problem”. When solving the Euler equation in the rest frame of a moving cell, the local velocity of the flow is irrelevant for the outcome of the calculation. This can be a great advantage when simulating moving discs in binary or multiple stellar systems.

The study closest to our work is Shen et al. (2010), where the authors performed fully self-gravitating simulations of gas discs encounters using SPH. Similarly to Lin et al. (1998), Shen et al. (2010) focused on the formation of self-gravitating objects (in the brown dwarf range) in tidal tails (reminiscent of the work of Barth 1992) and in compression shocks during encounters of very massive discs (the values of star mass, disc mass and disc radius used are  $M_* = 0.6 M_\odot$ ,  $M_d = 0.4 M_\odot$  and  $R_d = 250$  AU in Lin et al. 1998, and  $M_* = 0.5 M_\odot$ ,  $M_d = 0.6 M_\odot$  and  $R_d \sim 1000$  AU in Shen et al. 2010). In this work, we model discs of more moderate – and more plausible – masses (10% of the mass of the star), focusing on the role of the tidal forces on the orbital evolution of the host stars, and exploring how small the impact parameter must be in order to cause a significant change to the original orbits.

### 2.2 The AREPO code

AREPO (Springel 2010a, 2011) is a second-order finite-volume Godunov code that solves the equations of hydrodynamics on a moving mesh. This approach is built upon the idea that control volumes can be identified with the polygons/polyhedra of a Voronoi tessellation, which in turn is constructed from a set of *moving* mesh-generating points. Since a Voronoi tessellation changes continuously for smooth spatial trajectories of the generating points, each cell can be regarded as a “quasi-Lagrangian fluid parcel” (e.g., see Vogelsberger et al. 2012). Besides ideal hydrodynamics coupled to self-gravity, the code currently includes routines for magneto-hydrodynamics (Pakmor, Bauer & Springel 2011; Pakmor & Springel 2013; see also Mocz et al. 2014 and Mocz, Vogelsberger & Hernquist 2014), physical viscosity (Muñoz et al. 2013), radiative transfer in different approximations (Petkova & Springel 2011;

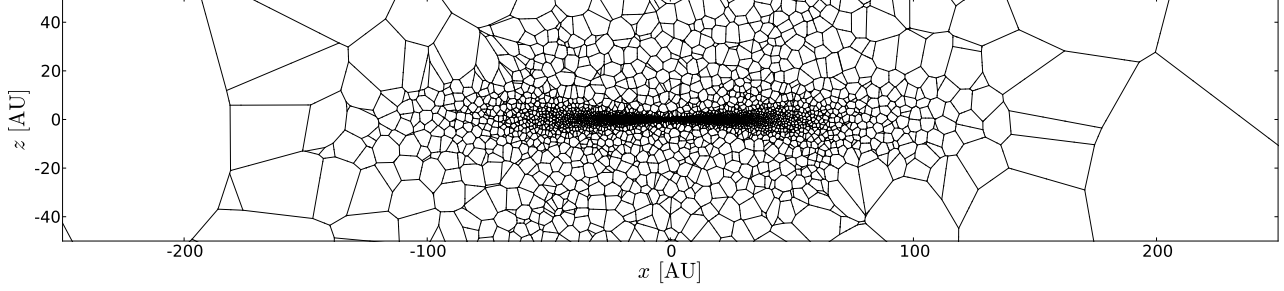


**Figure 1.** Slice through the mesh of a disc model, showing the transition between a mass-based sampling within the disc and a volume-based sampling in the background.

Sales et al. 2014), as well as numerous sub-resolution prescriptions for galaxy formation physics (Vogelsberger et al. 2013).

As in any unsplit, second-order, finite-volume method (see e.g., Toro 2009), the hyperbolic Euler equations are discretized for the  $i$ -th cell as (Springel 2010a):

$$\mathbf{Q}_i^{(n+1)} = \mathbf{Q}_i^{(n)} - \Delta t \sum_j A_{ij} \hat{\mathbf{F}}_{ij}^{(n+1/2)}, \quad (1)$$

where  $\mathbf{Q}$  is the volume integral of the state vector  $\mathbf{U} = (\rho, \rho\mathbf{v}, \rho e)$  (i.e., mass, momentum and energy densities),  $A_{ij}$  is the area of the face shared by the  $i$ -th and  $j$ -th cells and  $\hat{\mathbf{F}}_{ij}^{(n+1/2)}$  is a time-centered, area-averaged estimate of the flux vector  $\mathbf{F}_{ij}$ , which is an analytic function of the fluid variables.

However, since the Voronoi cells are moving, the flux  $\mathbf{F}_{ij}$  exchanged between the  $i$ -th and  $j$ -th cells needs to take into account the velocity  $\mathbf{w}$  of a moving boundary:

$$\begin{aligned} \mathbf{F}_{ij} &= \frac{1}{A_{ij}} \int_{A_{ij}} [\mathbf{F}(\mathbf{U}) - \mathbf{U}\mathbf{w}^T] d\mathbf{A}_{ij} \\ &\approx \hat{\mathbf{F}}_{ij} = \mathbf{F}(\mathbf{U}_{ij}) - \mathbf{U}_{ij}\mathbf{w}_{ij}^T \end{aligned} \quad (2)$$

where the state vector estimate  $\mathbf{U}_{ij}$  is obtained from the solution of a Riemann problem at the centroid of the interface and  $\mathbf{w}_{ij}$  is the velocity of the face centroid. This Riemann problem is solved on the frame of the moving face, and thus errors associated with this operation are independent of the magnitude of  $\mathbf{w}_{ij}$ . As a consequence, the truncation error in Equation (1) is velocity independent, a property that guarantees that the diffusivity and numerical noise in our disc simulation is independent of how fast they are moving across the computational domain. In addition, this approach allows for longer time steps, since the Courant condition is applied in the frame of the moving cell, and not in lab frame coordinates. This minimizes the numerical diffusion that would arise from taking many time-steps per dynamical time.

Gravity in AREPO is included as a source term to the right hand side of Equation (1). Integration of this term is carried out by a modified operator-splitting approach (Springel 2010a). For self-gravitating systems, the gravitational force is calculated using a hierarchical octree algorithm (Barnes & Hut 1986). All the simulations presented in this work are self-gravitating.

Because of the discretization of the equations of motion in cartesian coordinates, and the use of an octree algorithm for the gravitational force, in its current formulation AREPO does not conserve angular momentum to machine precision, but future modifications to the AREPO algorithm may improve the code's performance in this regard, enabling integration for longer timescales

than the ones used in this work<sup>1</sup>. For the disc models used here (see Section 2.3 below) and integration times of our runs, angular momentum conservation is satisfied to within 1%, which should not strongly influence our conclusions. Note that a significant amount of the observed angular momentum variability is due to the accretion of gas by the stars (we use a rather aggressive sink particle algorithm acting over a sphere of radius  $r_{\text{acc}} = 1$  AU around each star), which amounts to  $\dot{M}_* \gtrsim 10^{-7} M_\odot \text{ yr}^{-1}$ . A benefit of the moving-mesh approach is that, this error in angular momentum is independent of the disc bulk motion, which allows us to experiment with encounters at different speed without the need of adapting the resolution accordingly.

### 2.3 Circumstellar disc models

The moving-mesh code AREPO was benchmarked by Muñoz et al. (2014) for circumstellar disc simulations in 2-D, finding good agreement with other popular grid codes used for two-dimensional calculations of planet-disc interaction. In this work, we tackle the much more challenging problem of modeling full three-dimensional discs of finite extent in stationary equilibrium. We use a basic, observationally-justified model, which consists of a self-consistent, self-gravitating solution for a disc with a surface density distribution that satisfies the Lynden-Bell–Pringle model (Lynden-Bell & Pringle 1974):

$$\Sigma(R) = (2-p) \frac{M_d}{2\pi R_c^2} \left(\frac{R}{R_c}\right)^{-p} \exp\left[-\left(\frac{R}{R_c}\right)^{2-p}\right], \quad (3)$$

where  $M_d = 0.05 M_\odot$ ,  $p = 1$ ,  $R_c = 20$  AU and a stellar mass of  $M_* = 0.45$  is used for all our numerical experiments unless otherwise noted. These characteristic radii are consistent with the protoplanetary disc surface density profiles fitted from submillimeter observations by Andrews et al. (2009) using Equations (3) (these authors find a wide spread in  $R_c$ , going from  $\sim 20$  to  $\sim 200$  AU). Our models are comparable in size and mass to those by Forgan & Rice (2009), who chose outer disc radii of 40 AU and star and disc masses of  $M_* = 0.5 M_\odot$  and  $M_d = 0.07 M_\odot$  respectively.

Although the disc's characteristic radius  $R_c$  (Equation 3 defines the scale at which the disc surface density profile transitions from power-law form to an exponential cutoff), it does not define a specific disc *size*. We define  $R_d$  simply as the radius that encloses

<sup>1</sup> See Pakmor, Muñoz and Springel (in preparation) for a detailed analysis of the conservation and diffusion of angular momentum in moving-mesh hydrodynamics, including new schemes that may improve the code's performance in this regard.

95% of the disc mass. For a surface density profile given by Equation (3), it can be shown that the enclosed mass at radius  $R$  is

$$M_d(< R) = M_d \left\{ 1 - \exp \left[ - \left( \frac{R}{R_c} \right)^{2-p} \right] \right\}, \quad (4a)$$

$$\text{with } M_d(< R_d) \equiv 0.95 M_d. \quad (4b)$$

For  $p = 1$ ,  $R_d \approx 3R_c$ , i.e. the disc size is approximately 60 AU in our models.

Simulations are carried out by discretizing the 3-D volume into cells (Voronoi polyhedra) with a mass resolution of  $9 \times 10^{-7} M_\odot$  (0.3 Earth masses) except for those dilute regions outside the discs, where a cell volume ceiling is imposed. This implies that our fiducial  $0.05 M_\odot$  discs are described by  $\sim 500000$  cells, while more massive discs contain a larger number of resolution elements. Figure 1 shows a vertical slice of the Voronoi mesh, crossing the disc at its centre. The smooth transition from a dense mesh into a coarse background mesh can be clearly seen. A detailed explanation of the initial conditions and mesh-generation can be found in Appendix A. These initial conditions are very quiet: when discs are evolved in isolation, the projected surface density remains to be well represented by Equation 3 over a significant fraction of the integration time of our simulations (5000 years). Therefore, a relaxation stage of our initial conditions (which is very common in SPH simulations) is not necessary and it is not carried out here.

In addition to the density profile of Equation (3), a temperature profile is required to completely specify the vertical structure of the disc. For all models presented in this work, the temperature profile follows a power law  $T \propto R^{-l}$  with fixed  $l = 1/2$ , which corresponds to a mildly flared disc. The aspect ratio of the disc as a function of radius is set by the normalization of the temperature profile. The sound speed profile is a *fixed* function of stellocentric distance, and is satisfied at all times as the discs move across the computational domain (as done by Shen et al. 2010). We have employed two ways of enforcing this “local isothermality”. One way is to ignore the energy conservation equation and solve the Euler equations (1) using an iterative isothermal Riemann solver with a *space-varying* sound speed (e.g., as done in Muñoz et al. 2014). An alternative is to solve the energy equation with an ideal-gas equation of state setting the adiabatic index to be  $\gamma = 1 + \epsilon$  with  $\epsilon \ll 1$ . Of course, this is a reasonable shortcut if the discs do not exchange mass during the encounter, since this approximation implies that gas parcels preserve their initial temperature along Lagrangian trajectories: gas is not allowed to heat (or cool) if its stellocentric distance changes (see discussion on this issue in Muñoz et al. 2014). In addition,  $\epsilon$  needs to be small enough to counteract adiabatic shock heating. For example, for gas shocked at a Mach number of 30,  $\epsilon$  needs to be smaller than  $3 \times 10^{-5}$  for the post-shock temperature to be within 1% of the pre-shock temperature<sup>2</sup>. We have tested our runs using  $\gamma = 1 + 10^{-5}$ , plus a temperature relaxation term of the form  $\dot{T} = -(T - T_0)/\tau_{\text{cool}}$  with a cooling time  $\tau_{\text{cool}}$  equal to the local time-step. This additional source term in the energy equation allows for quick cooling/heating toward a reference temperature  $T_0$  that is set by the distance to the closest star. The benefit of this second approach is that more general/realistic cooling functions can be

<sup>2</sup> For a gas with adiabatic index  $\gamma = 1 + \epsilon$  and upstream temperature  $T_1$ , the temperature jump condition given a Mach number  $M_1$  is

$$T_2/T_1 \approx \frac{1}{2} (\epsilon M_1^2 + 2). \quad (5)$$

tested by simply changing  $\gamma$  and the cooling time, such that cooling/heating is delayed rather than “instantaneous”. For the results presented in this work, no significant difference has been measured when trying these two different cooling approaches.

Our numerical scheme calculates the gas self-gravity and thus is able to capture disc fragmentation and object formation. However, the disc masses involved in our study make fragmentation much less likely than for the models of Shen et al. (2010). None of the simulations performed for this work produce long-lived fragments. We have checked that, with cooler discs (temperatures scaled down by a factor of two or more), fragmentation is indeed possible (note that isothermal gas can be compressed by shocks to arbitrarily high densities). However, our choice of temperature is physically motivated and consistent with observations (see, e.g., Kratter, Matzner & Krumholz 2008; Kratter, Murray-Clay & Youdin 2010). The disc scale height is reasonably small ( $H/R = 0.1$  at the disc characteristic radius) and the temperatures only reach a maximum of  $\sim 300$  K when within 0.8 AU ( $\approx$  the softening length of the stellar potential) and reach a floor temperature of 10 K at roughly 100 AU from the central star. The minimum Toomre parameter in this disc model is  $Q_{\text{T,min}} \approx 4.5$ , and is reached at  $R = 15$  AU. Thus, we expect discs to be gravitationally stable during flyby encounters, except for those with nearly radial orbits (not explored here) which can compress disc mass without first removing it by action of tidal forces.

The absence of fragmentation ensures that our runs are not bogged down by the courant condition inside a dense fragment. It also simplifies the analysis of our results. The main focus of this work is the orbital evolution of the stars following an encounter. Since the torque exerted on the stars by the disc gas depends on the mass distribution and not on the gas temperature, the results should not depend on whether or not a disc forms secondary objects, unless of course that owing to low temperature (low Toomre  $Q$ ) the fragmentation is so violent that the entire disc is turned into a few small objects.

## 2.4 Impulsively-started tidal forces

Two relations are essential for determining the importance of tidal effects in disc-disc interactions. The first is the ratio between the disc size  $R_d$  and the pericenter distance between the two stars  $r_p$ . The second is the ratio between the disc’s internal angular momentum  $L_{\text{disc}}$  and the binary system’s orbital angular momentum  $|\mathbf{L}_{\text{orb}}|$ . If  $r_p \gg R_d$  and  $|\mathbf{L}_{\text{orb}}| \gg L_{\text{disc}}$ , tidal effects should be negligible and the stellar orbits should approximately evolve as those of point particles with mass equal to  $M_* + M_d$ .

The disc internal angular momentum (measured with respect to the centre of mass of the star+disc system),  $L_{\text{disc}}$ , can be computed analytically assuming that the azimuthal velocity field  $v_\phi$  is well approximated by the Keplerian value  $v_K$ . For  $p = 1$ ,

$$\begin{aligned} L_{\text{disc}} &\approx 2\pi \int_0^\infty v_K(R) \Sigma(R) R^2 dR \\ &= \frac{\sqrt{\pi}}{2} M_d \sqrt{GM_* R_c}, \end{aligned} \quad (6)$$

which is approximately  $0.835 M_\odot \text{ AU}^2 \text{ yr}^{-1}$ . Computing  $L_{\text{disc}}$  from our 3D numerical models by directly summing over all cells gives a value of  $L_{\text{disc}} \approx 0.85 M_\odot \text{ AU}^2 \text{ yr}^{-1}$ .

Another quantity of interest is the disc’s total energy  $E_{\text{disc}}$  (consisting of the disc’s total kinetic energy, the total gravitational binding energy, and the total thermal energy). Since our simulations

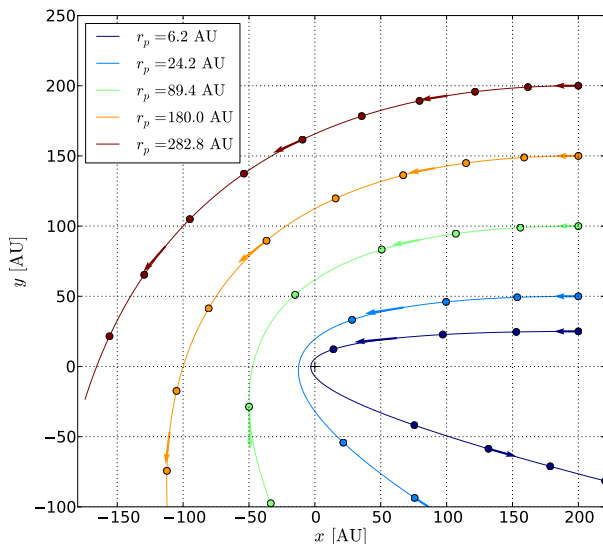


**Figure 2.** Orbital configurations explored in this work (for clarity, only one component of the binary is shown). Five different parabolic orbits are set up with five different pericenter separations, which take values  $r_p = 6.2, 24.2, 89.4, 180.0$  and  $282.8$  AU. Initial conditions start from the right of the figure at  $x = -200$  AU for *all* modeled orbits (conversely, the binary component not shown here is started at  $x = 200$  AU) with velocity along the  $x$ -axis. Orbital properties at  $t = 0$  are calculated assuming each disc is a point particle of mass  $0.5M_\odot$ . The magnitude of the velocity—chosen such that the orbit is parabolic for given an initial disc separation—ranges from  $\sim 1.7$  km s $^{-1}$  to  $\sim 2.1$  km s $^{-1}$ . The filled circles depict the locations for each trajectory in 200-year intervals.

are initialized with the stars on parabolic orbits (see Section 2.5 below), the orbital energy of the system should be strictly zero in the limit of zero tidal effects, i.e., when the star+disc trajectories can be accurately represented by those of point particles. Therefore, any discrepancy between the total energy of the binary system at  $t = 0$  and twice the value of  $E_{\text{disc}} \approx 0.24 M_\odot \text{ AU}^2 \text{ yr}^{-2}$  provides an indication of the tidal forces at startup and quantifies the validity of assigning point-mass trajectories to the disc-gas in the initial conditions.

## 2.5 Orbital configurations

Two identical copies of the fiducial disc presented in Section 2.3 are used to set up a parabolic encounter. Consequently, the orbital energy of the binary is  $E_{\text{orb}} = 0$ . The orbital plane of the encounter coincides with  $x$ - $y$  plane and the star-disc bulk initial velocities are directed along the  $x$ -axis (the discs directed toward each other). Therefore, the only free parameter is the pericenter separation  $r_p$ . Figure 2 shows the initial trajectories of one of the discs for five different values of  $r_p$ : 6.2, 24.2, 89.4, 180.0 and 282.8 AU. We call these different parabolic orbit configurations ‘PARA1’, ‘PARA2’, ‘PARA3’, ‘PARA4’ and ‘PARA5’ respectively. In addition, we vary the orientation of the discs with respect to the orbital angular momentum vector (angles  $\theta_1$  and  $\theta_2$ ). We also vary the disc orientations in seven different configurations, which are labeled accordingly by appending a number to the orbital label, e.g., ‘PARA1-1’, ‘PARA1-2’, etc. Table 1 shows the main set of simulations and their respective orbital and orientation parameters. Each orbital configuration (set by the value of  $r_p$ ) contains seven variants, which correspond to different combinations of the

angles  $\theta_1$  and  $\theta_2$  (same notation as Shen et al. 2010). The azimuthal orientation of the discs (angles  $\phi_1$  and  $\phi_2$ ) is not changed.

The orbital angular momentum in the two-body problem is  $\mathbf{L}_{\text{orb}} = m\sqrt{\mu r_p(1+e)}\hat{\mathbf{z}}$  where  $m = M_1 M_2 / (M_1 + M_2) = 0.25M_\odot$  is the reduced mass and  $\mu = GM_{\text{tot}}$  where the total mass is  $M_{\text{tot}} = 1M_\odot$ . The seventh column in Table 1 shows the orbital angular momentum of each simulation according to the chosen value of  $r_p$ . The eighth column shows the expected value of the  $z$ -component of the *total* angular momentum  $L_{\text{tot},z}$ , taking into account the contribution from the disc internal angular momentum; i.e., at time  $t = 0$ :

$$L_{\text{tot},z} = |\mathbf{L}_{\text{orb}}| + L_{\text{disc},1} \cos \theta_1 + L_{\text{disc},2} \cos \theta_2, \quad (7)$$

where  $L_{\text{disc},1} = L_{\text{disc},2} \approx 0.85 \text{ AU}^2 \text{ yr}^{-1}$  (Section 2.3). A comparison between  $|\mathbf{L}_{\text{orb}}|$  and  $L_{\text{tot},z}$  shows that the total angular momentum can be changed significantly by simply changing the orientation of the discs. From these quantities, we can estimate that the simulation subsets ‘PARA1’ and ‘PARA2’ should show a greater degree of redistribution of angular momentum between the gas and the stars (and produce capture) as well as a significant dependence of the simulation outcome on the orientation of the discs. Our initial conditions satisfy Equation (7) within less than a few percent, indicating that the superposition of two stationary, isolated disc models into a self-interacting binary system is reasonably adequate at the values of the initial separation  $D$  that we have chosen. We have noticed that the angular momentum error seeded on startup is slightly higher for the larger pericenter simulations. Although the discs in these simulations were started far apart (Figure 2) precisely to avoid these problems, it is worth pointing out that the angular momentum of the system grows faster with  $r_p$  than with  $D$ . For example, the ratio in  $D$  for the orbital configurations ‘PARA5’ ( $r_p = 282.8$ ) and ‘PARA1’ ( $r_p = 6.2$ ) is  $\sim 1.4$ , while the ratio in  $|\mathbf{L}_{\text{orb}}|$  for the same configurations is  $\sim 6.8$ . As a consequence, the errors in setting up the orbit are fractionally larger, albeit still small, for our wider orbits. Although the impulsive forces implied by this fractional error are still negligible for the dynamics of the encounter, we foresee some small complications arising from not setting up a configuration that is not sufficiently distant.

Similarly, the consistency between the measured energy at the zeroth snapshot and the expected energy derived from the superposition of two isolated disc models provides another measure of whether the initial conditions are quiet, or if the discs are so close that the tidal forces are imparted impulsively at the beginning of the simulation. The total energy of the system is  $E_{\text{tot}} = 2E_{\text{disc}} + K_{\text{orb}} + V_{\text{orb}}$ , but as we have mentioned above,  $K_{\text{orb}} + V_{\text{orb}} = E_{\text{orb}} \approx 0$ . Therefore, the total energy of the system, *regardless* of the pericenter distance, should be just twice the energy of the individual disc model:  $E_{\text{tot}} \approx -0.48 \text{ AU}^2 \text{ yr}^{-2}$ . Just as with  $L_{\text{tot}}$ , we find deviations of the order of 1–2%, indicating that some tidal forces are acting on the discs at  $t = 0$ .

## 3 RESULTS

### 3.1 Encounter morphology

Figures 3–5 show projected density images of 21 out of the 35 simulations listed in Table 1. These figures show rendered snapshots at some time after pericenter passage for simulation subsets ‘PARA1’, ‘PARA2’ and ‘PARA5’ (Table 1).

**Table 1.** Orbital parameters for parabolic encounters with different pericenter separations

Simulation	$r_p$ [AU]	$\theta_1$ [°]	$\phi_1$ [°]	$\theta_2$ [°]	$\phi_2$ [°]	$ \mathbf{L}_{\text{orb}} $ [ $M_\odot \text{ AU}^2 \text{ yr}^{-1}$ ]	$L_{\text{tot},z}$ [ $M_\odot \text{ AU}^2 \text{ yr}^{-1}$ ]	$M_d/M_*$	disc-orbit alignment <sup>a</sup>	Capture (C) or fly-by (FB)
PARA1-1_M2	6.2	0	0	0	0	5.53	7.23	0.05/0.45	P-P	FB
PARA1-2_M2	"	0	0	45	0	"	6.98	"	P-P	C
PARA1-3_M2	"	0	0	90	0	"	6.38	"	P-P	C
PARA1-4_M2	"	0	0	135	0	"	5.78	"	P-R	C
PARA1-5_M2	"	0	0	180	0	"	5.53	"	P-R	C
PARA1-6_M2	"	180	0	180	0	"	3.83	"	R-R	C
PARA1-7_M2	"	180	0	135	0	"	4.08	"	R-R	C
PARA2-1_M2	24.2	0	0	0	0	10.9	12.6	0.05/0.45	P-P	FB
PARA2-2_M2	"	0	0	45	0	"	12.4	"	P-P	FB
PARA2-3_M2	"	0	0	90	0	"	11.8	"	P-P	FB
PARA2-4_M2	"	0	0	135	0	"	11.2	"	P-R	FB
PARA2-5_M2	"	0	0	180	0	"	10.9	"	P-R	C
PARA2-6_M2	"	180	0	180	0	"	9.23	"	R-R	C
PARA2-7_M2	"	180	0	135	0	"	9.48	"	R-R	C
PARA3-1_M2	89.4	0	0	0	0	21.0	22.7	0.05/0.45	P-P	FB
PARA3-2_M2	"	0	0	45	0	"	22.5	"	P-P	FB
PARA3-3_M2	"	0	0	90	0	"	21.9	"	P-P	FB
PARA3-4_M2	"	0	0	135	0	"	21.3	"	P-R	FB
PARA3-5_M2	"	0	0	180	0	"	21.0	"	P-R	FB
PARA3-6_M2	"	180	0	180	0	"	19.3	"	R-R	FB
PARA3-7_M2	"	180	0	135	0	"	19.6	"	R-R	FB
PARA4-1_M2	180.0	0	0	0	0	29.8	31.5	0.05/0.45	P-P	FB
PARA4-2_M2	"	0	0	45	0	"	31.3	"	P-P	FB
PARA4-3_M2	"	0	0	90	0	"	30.7	"	P-P	FB
PARA4-4_M2	"	0	0	135	0	"	30.1	"	P-R	FB
PARA4-5_M2	"	0	0	180	0	"	29.8	"	P-R	FB
PARA4-6_M2	"	180	0	180	0	"	28.1	"	R-R	FB
PARA4-7_M2	"	180	0	135	0	"	28.4	"	R-R	FB
PARA5-1_M2	282.8	0	0	0	0	37.4	39.1	0.05/0.45	P-P	FB
PARA5-2_M2	"	0	0	45	0	"	38.8	"	P-P	FB
PARA5-3_M2	"	0	0	90	0	"	38.2	"	P-P	FB
PARA5-4_M2	"	0	0	135	0	"	37.6	"	P-R	FB
PARA5-5_M2	"	0	0	180	0	"	37.4	"	P-R	FB
PARA5-6_M2	"	180	0	180	0	"	35.7	"	R-R	FB
PARA5-7_M2	"	180	0	135	0	"	35.9	"	R-R	FB

<sup>a</sup> disc-orbit alignment is classified into prograde-prograde (P-P), prograde-retrograde (P-R) or retrograde-retrograde (R-R) based on the orientation angles  $\theta_i$  with  $i = 1, 2$  (prograde if  $\theta_i \leq 90^\circ$  and retrograde if  $\theta_i > 90^\circ$ ).

Simulation sets 'PARA1' and 'PARA2' have pericenter distances of  $r_p = 6.2$  and  $24.2$  AU respectively, and therefore we expect the greatest disruption to the gas discs in these simulation sets due to tidal effects but also due to direct shock-induced truncation. The disc models have characteristic radii of  $R_c = 20$  AU and outer radii of  $R_d = 60$  AU (Section 2.3), and thus the discs are expected to collide directly (i.e.,  $r_p/2 < R_d$ ) for configurations 'PARA1', 'PARA2' and 'PARA3'. However, for 'PARA3', the enclosed mass at  $R = r_p/2 = 44.7$  is 89% of the disc total mass, and thus, despite the evident disc truncation seen in Figure 4 (note that the projected density range spans nearly 5 orders of magnitude), this encounter should have little effect on the stellar orbits.

Indeed, two different regimes can be clearly distinguished from the evolution of the stellar orbits. Figure 3 shows significant disruption of the gas distribution, as well as changes in the orbit of the stars. In contrast, figure 4 shows some disc truncation and strong tidal features, but the disc centres (approximately the position of the stars) show no distinguishable variation from

frame to frame, i.e., the orientation of the discs bears little importance. The response of the orbits depends weakly on the extended mass distribution thus the evolution can be reasonably approximated by two point masses. Figure 5 shows little to no modification in the disc surface density besides the excitation of  $m = 2$  spiral arms, which are characteristic of tidal encounters (e.g. Binney & Tremaine 2008; D'Onghia et al. 2010). Evidently, the steepness of the tidal force with distance can explain the rapid change in output with  $r_p$  (the calculations of Ostriker 1994 show an exponential dependence of the energy change in  $(r_p/R_d)^{3/2}$ ).

Another indication of the rapidly decreasing influence of the disc is the presence of some tidal features. We can see the same tidal features arise in disc #1 in the first five panels of Figure 4 and 5 (morphological similarities are harder to find in Figure 3). These features arise independently of the orientation and shape of disc #2 (the orientation of disc #1 is unchanged for the first five runs of each simulation subset in Table 1). This is an indication that, to first order, the tidal features depend on the monopole component of

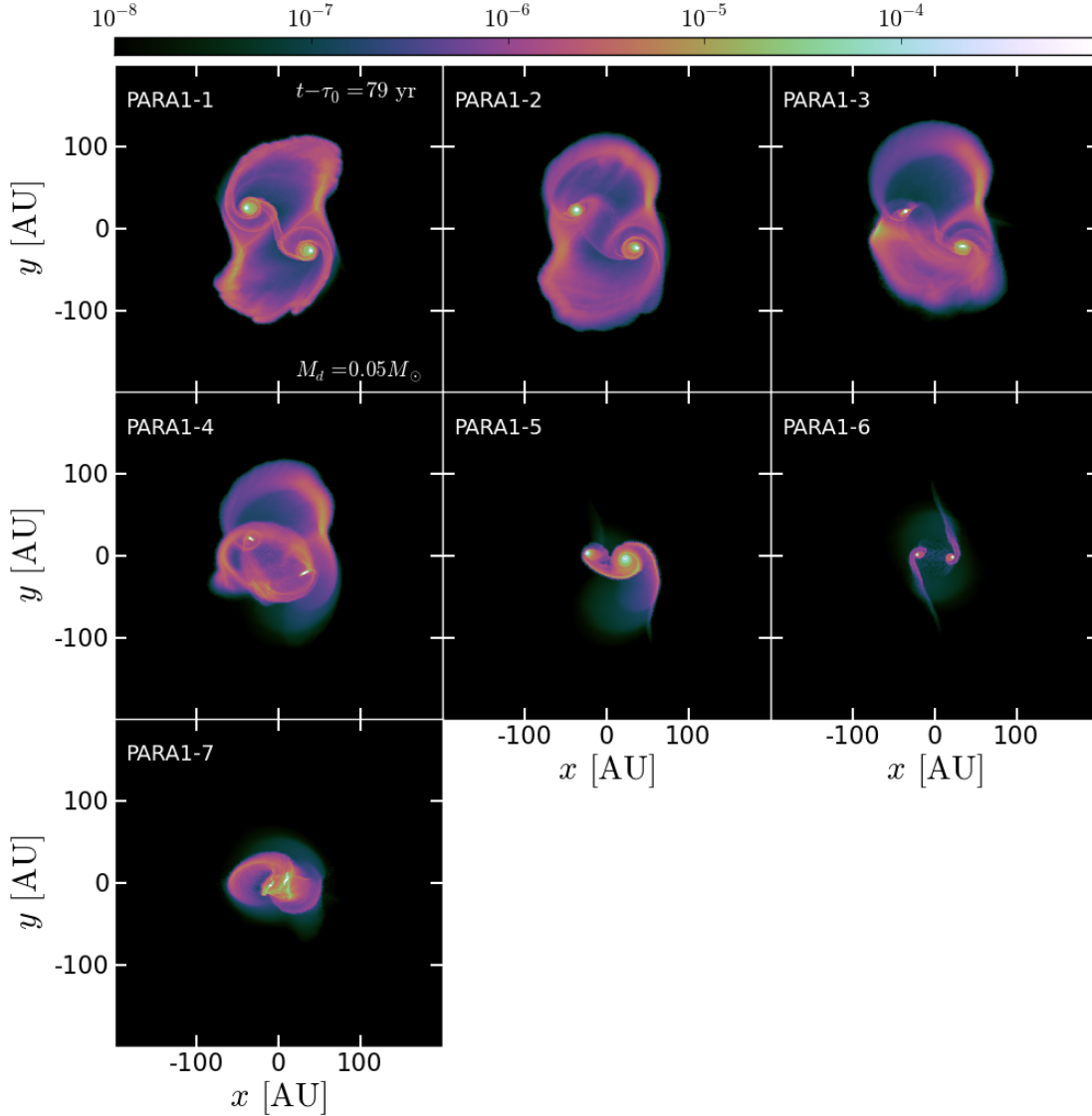


**Figure 3.** Simulation output for the orbital set ‘PARA1’ ( $r_p = 6.2$ ) a short time after pericenter passage ( $t - \tau_0 = 79$  yr), which corresponds to a simulation time of 700 yr. Six out of these seven simulations show orbital capture before the end of the integration (5000 years), meaning that the stars came back for at least one more pericenter passage (see text). Each frame shows the projected density in units of  $M_\odot \text{AU}^{-2}$  (the conversion factor to  $\text{g cm}^{-2}$  is  $8.88 \times 10^6$ ). All images are generated by integrating the three-dimensional density field along one direction following the full Voronoi mesh.

the companion’s potential (strongly dominated by the central star), even as significant mass stripping has taken place due to the physical collision of the discs.

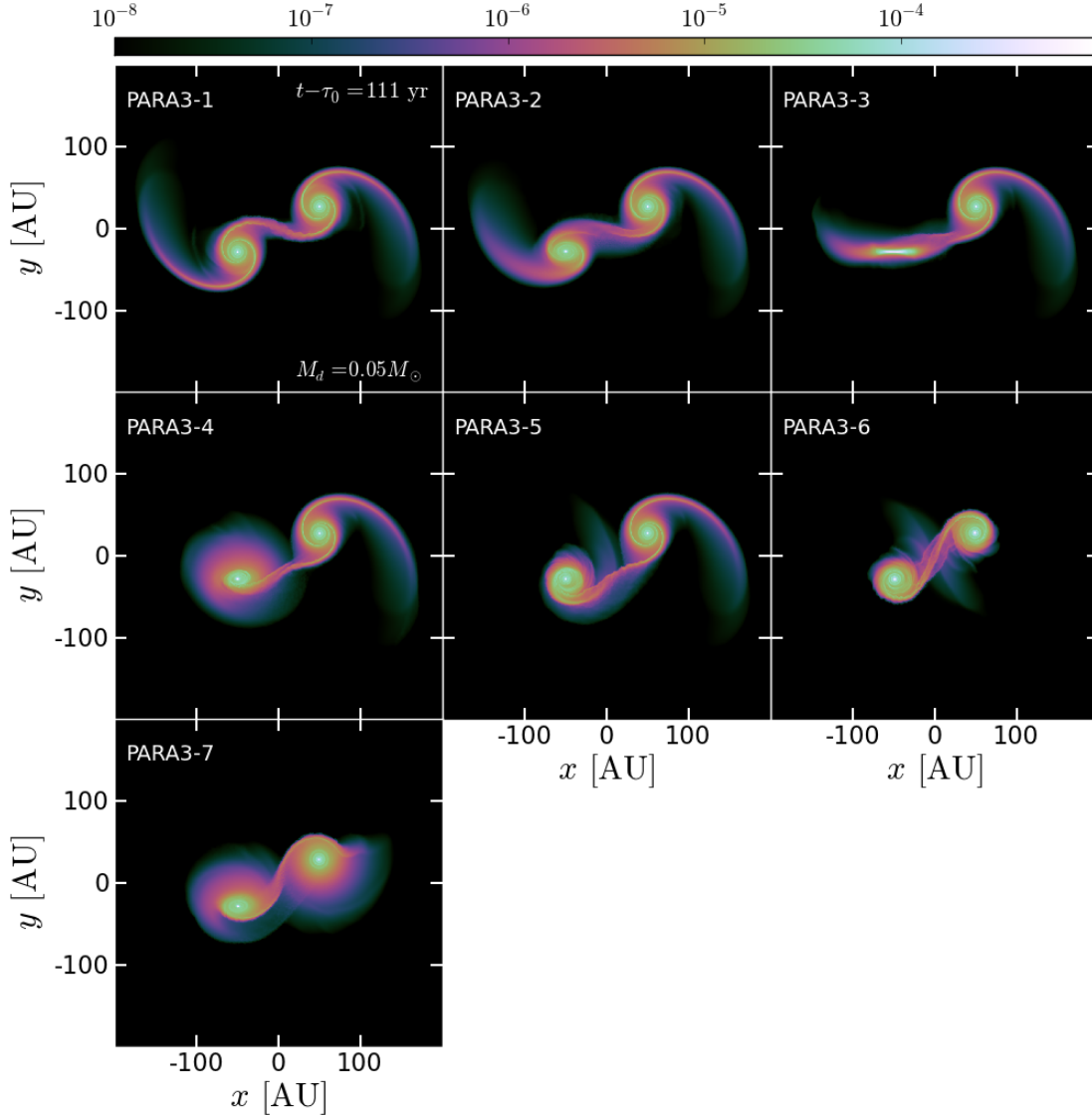
### 3.2 Stellar orbits

Figure 6 shows the inter-star separation for the most disruptive set of orbits (‘PARA1’). At pericenter passage, all orbits suffer a significant energy loss that shrinks the semi-major axis compared to the initial parabolic trajectory. Before pericenter (i.e.,  $t < 621$  yrs) all runs follow the analytic trajectory closely, and reach pericenter at the same time. After pericenter, the orbital evolution varies dramatically among these configurations. In six of the runs, there are at least three additional close pericenter passages and over  $\sim 50$  additional ones in the most disruptive configuration. Based on these additional separation minima we categorize these systems as “captured.” The seventh configuration (‘PARA1-1’) hints that the stellar separation has reached apocenter at the end of the simulation, and that it should go back for a second passage at around

$t = 7000$  yr. Consequently, all simulations in the set ‘PARA1’ show sufficient energy loss to be considered bound after first passage.

The different outcomes of the ‘PARA1’ simulations are determined by the relative orientation of the discs. Each curve in Figure 6 is labeled according to a normalized  $z$ -spin value  $S_z \equiv \cos \theta_1 + \cos \theta_2$ . Prograde-prograde encounters like ‘PARA1-1’, ‘PARA1-2’ and ‘PARA1-3’ contain a larger amount of angular momentum than the prograde-retrograde and the retrograde-retrograde encounters. Configurations that include one or two discs in retrograde orientation will result in different torques on to the stars since the initial response of the gas to first passage will be different. Retrograde orientations do not contain orbital resonances (e.g. Toomre & Toomre 1972; D’Onghia et al. 2010), and extended spiral arms are not formed as a result. The parabolic orbits in this models are chosen to model the first ever encounter between two objects (hyperbolic encounters were not considered in this work), and thus we do not expect a correlation between pericenter separation and mutual disc inclination. This is most likely not true





**Figure 4.** Simulation output for the orbital set ‘PARA3’ a short time after pericenter passage ( $t - \tau_0 = 111$  yr), which corresponds to a simulation time of 1000 yr. See description of Figure 3.

for bound orbits, however, since a common formation scenario for close binary stars would suggest that these are born with nearly aligned discs as they are with nearly aligned spins (see Hale 1994).

The orbital decay is almost entirely determined by the energy loss at first passage. Although the amplitude of the separation curve is observed to decay slowly in time, most of the dissipation happens at once when the discs first meet. This is not surprising given that configuration ‘PARA1’ has a pericenter distance ( $r_p = 6.2$ ) that is significantly smaller than the sum of the disc radii ( $2 \times R_d = 120$  AU). Thus, the first encounter violently truncates the disc on very short timescales, potentially reducing the mass of the disc by a factor of  $\sim 4$  (from Equation 4a,  $M_d(< 6.2 \text{ AU}) \approx M_d/4$ ), after which the tidal interaction goes back into a linear regime and the orbit evolves more slowly.

Figure 7 shows the evolution of stellar separation for the remainder of the simulations in our study, grouped by orbital configuration. The likelihood of capture decreases very rapidly with pericenter separation. Only three out of seven simulations in the ‘PARA2’ show additional pericenter passages (although all of them show substantial orbital energy loss). The runs in set ‘PARA3’ show a much weaker effect; although, as before, the

change in separation increases when  $S_z$  is decreased. The stars should not be expected to interact again for another few 10,000 yrs, and after reaching separations of a few to several thousand AU, meaning that these systems are not true “binaries”. In the case of ‘PARA4’ and ‘PARA5’, the interaction appears extremely weak, since stellar separations remain on their original parabolic trajectories with variations of the order of 1% toward the end of the simulation. These variations are attributable to other effects besides tidal interactions (e.g., numerical accuracy, lack of strict conservation of angular momentum, torque onto the stars by gas accretion, etc). Although the tidal response of the disc is clear in these last two examples, the long term effect on the orbits of the stars is negligible.

### 3.3 Orbital evolution

Although the stellar separation is informative, it does not describe completely the orbital evolution. In order to analyze the orbital evolution of each star+disc system, we need to assign them meaningful osculating elements. However, identifying which gas belongs to a disc and which is simply surrounding material is not a trivial task.



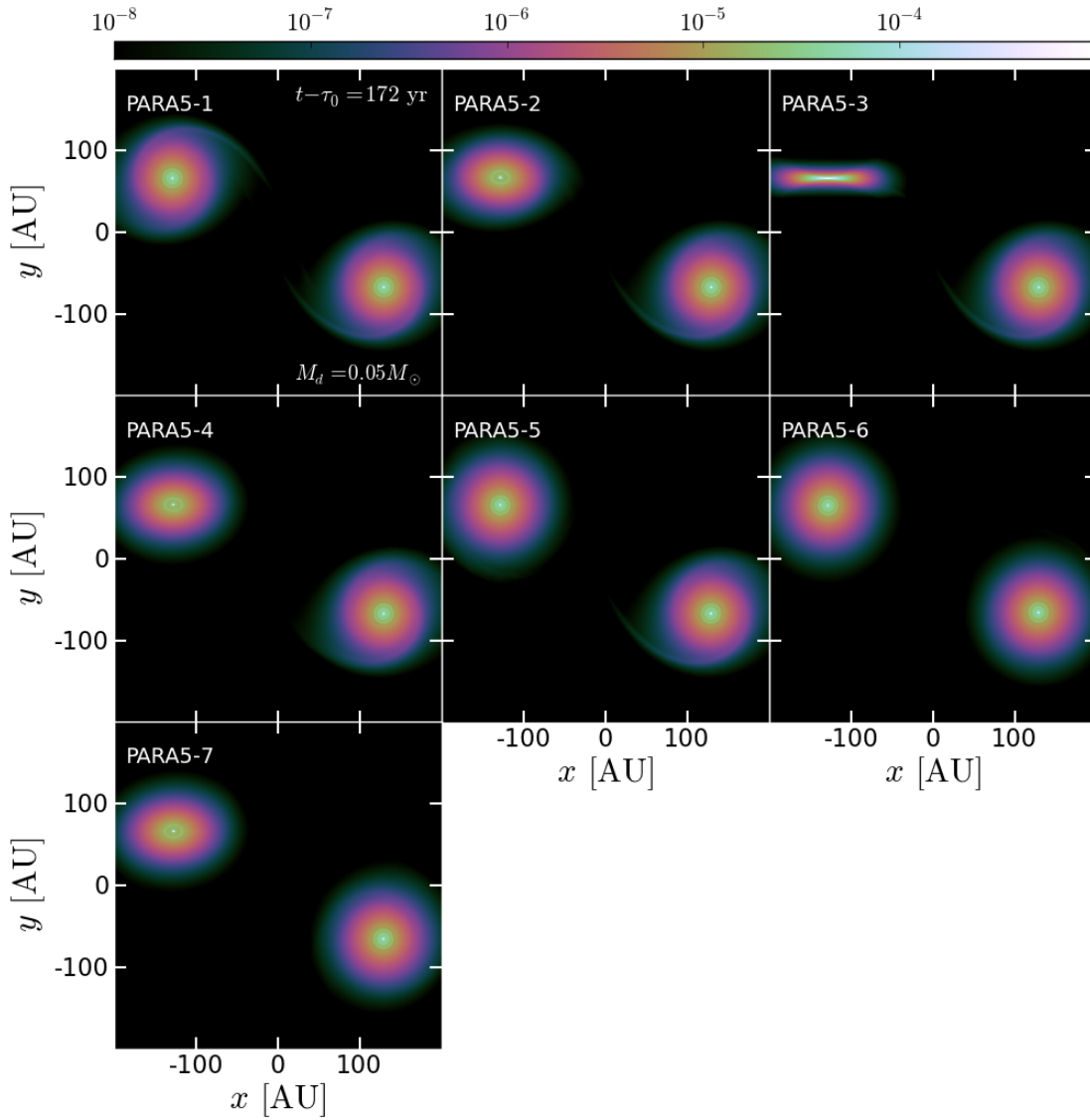


**Figure 5.** Simulation output for the orbital set ‘PARA5’ a short time after pericenter passage ( $t - \tau_0 = 172$  yr), which corresponds to a simulation time of 1600 yr. See description of Figure 3.

Although group finding algorithms abound in the literature, these are designed for heavily clustered distributions in space (this is the basis for halo-finding algorithms in cosmology; e.g., Davis et al. 1985). Although spatial density-based clustering algorithms might have little trouble identifying discs in configurations as in Figure 5, disordered gas distributions like that of Figure 3 likely present a challenge for automatized searches. For simplicity, we will consider as disc material all cells lying within each star’s Roche lobe (in this equal-mass example, delimited roughly by the midpoint between the two stars). Then, we proceed to identify all the mass within the chosen region, calculating its centre of mass and the centre of mass velocity. With these quantities, we define a classical two-body problem and calculate the orbital elements for each snapshot. Since over short timescales the dynamics should be dominated by the two stars (they contain 90% of the mass of the system), we expect this approximation to be a good first order indicator of the orbital evolution of the system.

Figure 8 shows the orbital elements calculated in the manner described above for a subset of the simulations. The pericenter time series show a markedly different behaviour between simulation sets ‘PARA1’ and ‘PARA2’ with respect to sets ‘PARA3’, ‘PARA4’ and ‘PARA5’. The former group shows substantial

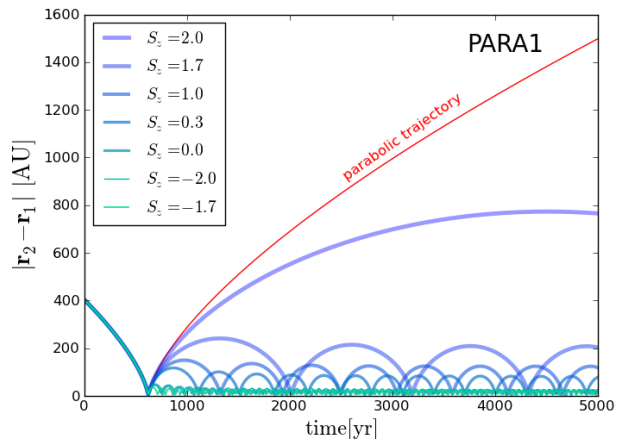


**Figure 6.** Time evolution of stellar separation in the ‘PARA1’ orbital configuration (seven distinct runs). Lines are labeled according to “normalized total disc spin” in the  $z$ -direction, defined as  $S_z = \cos \theta_1 + \cos \theta_2$ . If  $S_z = 2$ , both discs have spin angular momenta aligned with  $\mathbf{L}_{\text{orb}}$ , while a value of  $-2$  means that both spins are antiparallel with  $\mathbf{L}_{\text{orb}}$ . The simulation results show that the exactly parabolic initial trajectory (red line) is followed very closely by the stars until pericenter passage.

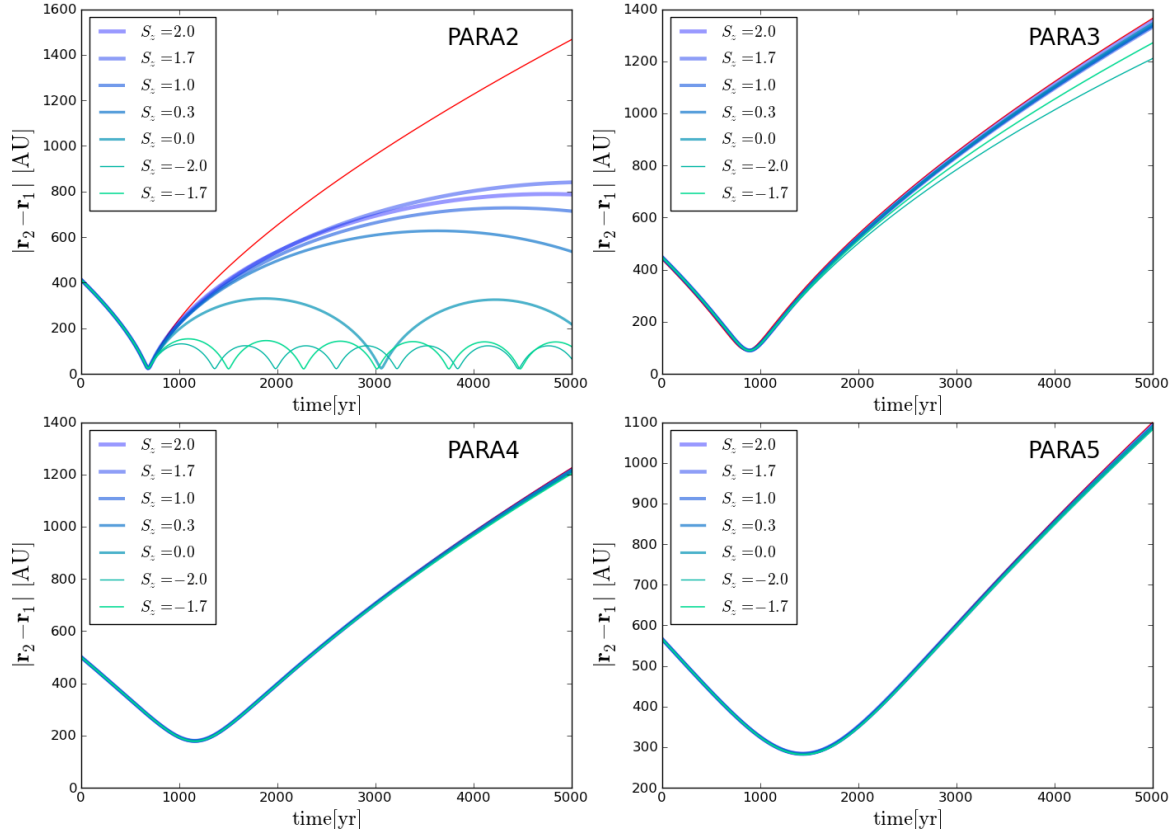


**Figure 7.** Same as Figure 6, but now for the ‘PARA2’, ‘PARA3’, ‘PARA4’ and ‘PARA5’ configurations. As before, the color of the curves is chosen according to the combined disc spin in each configuration

changes in  $r_p$  after pericenter (up to 50% in the case of ‘PARA1’), while the latter group shows a variability that could be consistent with a random walk behaviour. Smoother over timescales of  $\sim 1000$ , sets ‘PARA3’, ‘PARA4’ and ‘PARA5’ show little to no consistent trend in  $r_p$  as a function of time. The total  $\Delta r_p$  ranges from 1% – 2% in the case of ‘PARA3’, to  $\sim 0.1\%$  in the case of ‘PARA5’. The seemingly stochastic behaviour of  $r_p$  in this regimes leads us to conclude that the evolution is dominated by numerical noise or stochastic accretion due to our sink particle scheme and that the “true” small variability of  $r_p$  is buried (‘PARA4’ and ‘PARA5’) or partially buried (‘PARA3’) under noise.

The evolution of eccentricity shows a significant deviation from unity for sets ‘PARA1’ (up to 30%), ‘PARA2’ (up to 30%) and ‘PARA3’ (up to 6%). Even ‘PARA4’ and ‘PARA5’ (not shown), although again with a component of stochasticity, show a clear overall trend of decreasing eccentricity that flattens out toward the end of the simulation. The fact that the eccentricity reaches a finite value toward the end indicates that, despite the evident noise contamination, this loss of energy is real; furthermore, ‘PARA5’ flattens out later than ‘PARA4’, consistent with the fact that the pericenter timescale of ‘PARA5’ is longer and therefore the tidal interaction is expected to be spread over a longer time interval.

An interesting outcome of the pericenter evolution of ‘PARA1’ is that  $r_p$  grows after pericenter for positive values of  $S_z$  but decreases for  $S_z \leq 0$ . Therefore, although Figure 6 already hints at a loss of orbital energy (confirmed by the drop in  $e$  below 1 right after pericenter) the pericenter does not necessarily shrink. In principle, this effect can shield the discs from undergoing a second

disruptive pericenter passage of similar proximity to the first, now that the minimum distance has been increased. Conversely, those simulations with the most negative values of  $S_z$  show a decrease in the magnitude of pericenter distance after the first passage. These simulations (‘PARA1-6’ and ‘PARA1-7’) show several subsequent encounters, as if undergoing a runaway process in which each encounter facilitates the following one at an even smaller separation. This process could only stop once the gravitational softening lengths of the stars overlap (thus introducing an artificial “pressure”), or if the dispersal of the disc – via truncation or accretion – has made the tidal effects insignificant. Indeed all negative spin simulations in ‘PARA1’ end up stabilizing in  $r_p$ , although they do so at a time considerably longer than the timescale associated with pericenter passage.

Another feature observed in the first three orbital configurations and absent in ‘PARA4’ and ‘PARA5’ is the sharp increase in eccentricity right before pericenter. Note that for those orbits that were classified under “orbital capture” (Table 1), every subsequent pericenter passage is preceded by smaller glitches in eccentricity. Technically, this means that right before the orbit becomes elliptical it actually behaves briefly as a hyperbolic orbit. One must bear in mind that these orbital elements are proxies for what is actually happening with the (at time ill-defined) discs during the encounter, and that these values of  $r_p$  and  $e$  might not have much physical meaning when the gas is being entirely dispersed by a very violent interaction. Indeed, an important transition when going from ‘PARA3’ to ‘PARA4’ is that in the former case the discs actually come into contact, while in the latter there is no direct gas collision. Therefore, glitches in eccentricity observed right before

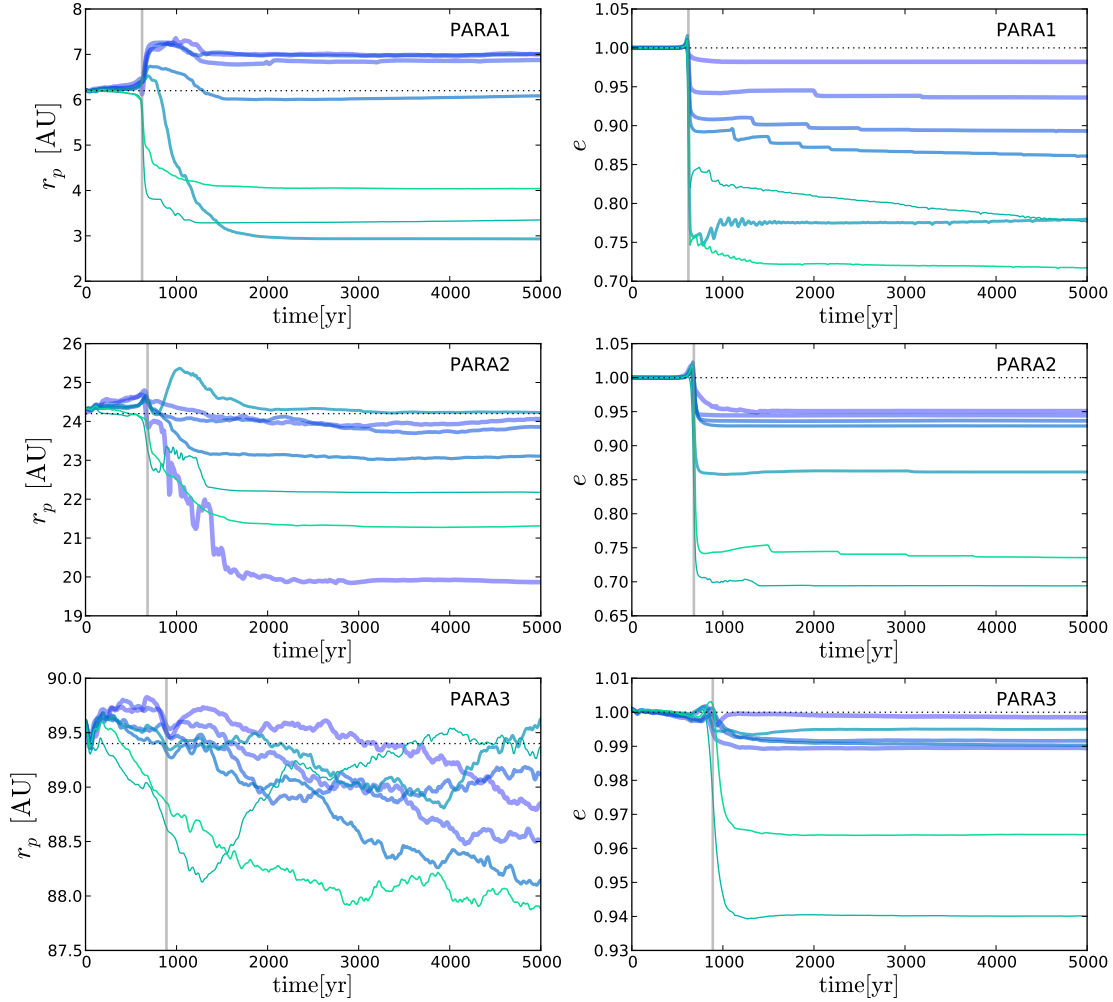


**Figure 8.** Time evolution of the orbital elements (pericenter separation  $r_p$  and eccentricity  $e$ ) for ‘PARA1–PARA3’ from Table 1 using the same color scheme as in Figure 7. ‘PARA4–5’ are omitted due to similarity with ‘PARA3’ as described in the text. The vertical gray lines mark the expected time of pericenter  $\tau_0$  based on the initial parabolic orbit for any given orbital configuration. The horizontal dotted line represents the initial value of  $r_p$  (Table 1) and eccentricity  $e$  ( $=1$  for all orbits).

a close encounter might be an exclusive outcome of disc-disc interactions mediated by shocks. Alternatively, the glitch in eccentricity for ‘PARA4’ and ‘PARA5’ is either too mild to be detected above the noise fluctuations or it simply should have taken place before the start of the simulation (see Section 3.4), which would explain why as opposed to the other orbital configurations, eccentricity in ‘PARA4’ and ‘PARA5’ is decreasing roughly monotonically in time since the beginning of the runs.

### 3.4 Orbital energy and angular momentum

To track the evolution of the binary orbits, we calculate the orbital energy  $E_{\text{orb}} = -GM_1M_2(1-e)/(2r_p)$  and orbital angular momentum  $|\mathbf{L}_{\text{orb}}| = M_1M_2\sqrt{Gr_p(1+e)/(M_1+M_2)}$  throughout the simulation, where  $M_1 = M_{*,1} + M_{d,1}$  and  $M_2 = M_{*,2} + M_{d,2}$ . This definition of orbital angular momentum is equivalent to separating the total angular momentum of the system  $\mathbf{L}_{\text{tot}}$  obtained by direct summation (disc cells and stars) into two components: the inner angular momentum of each disc and its host star  $\mathbf{L}_{\text{disc}}$  (measured with respect to the centre of mass of each star-plus-disc system, which is roughly the location of the star) and  $\mathbf{L}_{\text{orb}}$ .

Figure 9 shows  $E_{\text{orb}}$  normalized by  $GM_1M_2/r_p$  (left column) and  $|\mathbf{L}_{\text{orb}}|$  normalized by its value at  $t = 0$ . These figures share the same axes range to highlight the dramatic differences in energy and angular momentum change in the orbits. While ‘PARA1’ and ‘PARA2’ show substantial evolution, sets ‘PARA3’ through ‘PARA5’ change their orbital properties by very small amounts. The ‘PARA4’ and ‘PARA5’ runs also show good conservation of total angular momentum since tidal effects are small, and therefore triggered accretion is minimal (recall that some angular momentum can be lost owing to the accretion of rotating gas onto the stars). The change in  $L_{\text{tot},z}$  over  $\sim 3000$  years in the ‘PARA5’ runs ranges from  $-1\%$  to  $+0.5\%$ , which is as constant as observed in isolated discs.

The shaded region in Figure 9 defines the “interaction period” outside of which the tidal forces are expected to have very little effect. This window is defined as proportional to the pericenter timescale  $t_{\text{peri}} \equiv r_p/v_p = r_p/\sqrt{\mu/r_p}$ , where we use  $\mu = G \times 1M_{\text{tot}}$  with  $M_{\text{tot}} = 1M_{\odot}$ . Empirically, we find that a window of half-width equal to  $6 \times t_{\text{peri}}$  encloses most of the energy and angular momentum change centered around pericenter passage  $\tau_0$ . In practice, the interaction window has a width of  $\sim 40$  yrs for

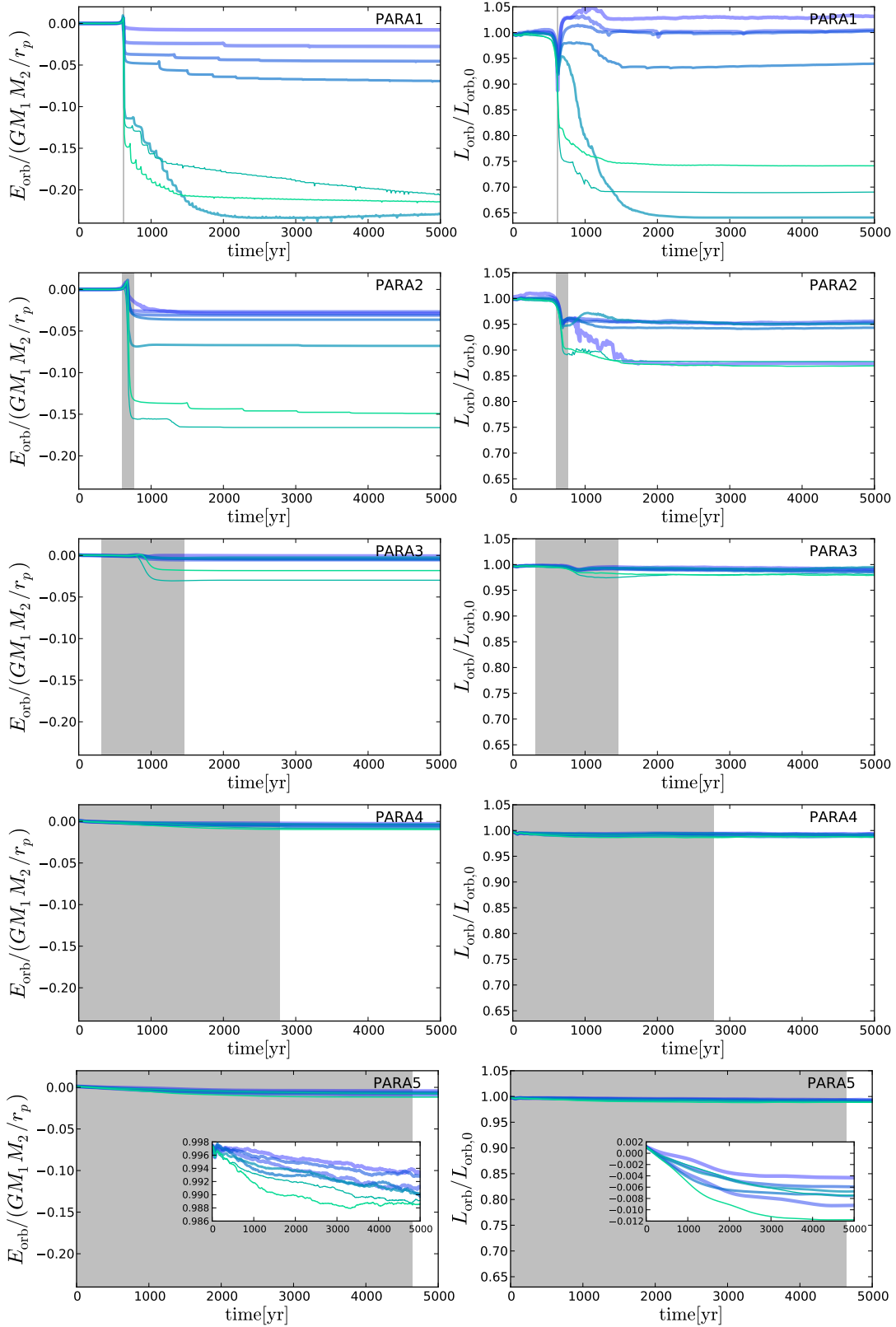


**Figure 9.** Orbital energy  $E_{\text{orb}}$  (left column) normalized by the reference value  $GM_1 M_2 / r_p$  and orbital angular momentum  $|L_{\text{orb}}|$  normalized by its initial value  $L_{\text{orb},0} = \frac{1}{4}$  for the 35 simulations of Table 1 using the same color scheme as in Figure 7. Each panel groups a subset of simulations of identical pericenter distance. The coordinate range in the  $y$ -axes is the same for all orbital configurations to highlight the dramatic difference in orbital evolution as  $r_p$  increases. The inset in the last row (orbital configuration 'PARA5') contains a zoomed in region showing that the change in  $E_{\text{orb}}$  and  $|L_{\text{orb}}|$  is less than 1%. The shaded region covers the "interaction period" centered around pericenter within which most of the energy and angular momentum exchange between the two discs takes place. 'PARA3' and 'PARA4' (not displayed) show variability of order 5%.

'PARA1' (i.e., consisting of only a handful of snapshots) and of  $\sim 4600$  yrs for 'PARA5', which covers nearly the full integration. Most importantly, the asymmetry of the total integration time with respect to pericenter time  $\tau_0$  implies that for very long interaction periods with half-lengths  $\gtrsim \tau_0$ , the tidal interaction preceding proper pericenter is not entirely captured by the simulation. This is the case in 'PARA4' and 'PARA5', for which the tidal interaction is expected to begin at wider separations than the ones included in our initial conditions (see discussion on the fractional error in orbital angular momentum in Section 2.5). It is possible that some of the differences between 'PARA4' and 'PARA5' as compared to the other orbital tests (for example, that there is no steep jump in eccentricity right before pericenter in Figure 9) could be due to an extremely wide tidal interaction window and that 'PARA4' and 'PARA5' are simply "incomplete", that is, their integration should have begun at greater separations in order to cover the asymptotic interaction.

### 3.5 Comparison to linear theory

The tidal interaction between a star+disc system and another stellar flyby was studied in detail by Ostriker (1994). Although that work focused on a simpler system containing only one disc, a comparison should be meaningful for our wide-separation simulations.

Assuming one disc changes orientation (in our simulations, the first five runs of each subset only differ in the value of  $\theta_2$ ) the angular momentum loss suffered by the victim disc is, in the linear regime (Eq. 3.1 in Ostriker 1994),

$$\Delta L_{\text{disc},2} = -C \left[ \cos \frac{\theta_2}{2} \sin \frac{\theta_2}{2} \right]^4 \left[ \frac{2}{\Omega(R_d)} \right] \left( \frac{3}{2} \right)^2 \left[ \cos \frac{\theta_2}{2} / \sin \frac{\theta_2}{2} \right]^4 \quad (8)$$

where the normalization factor

$$C = 2^3 \pi^2 G M_{*,2} R_d \Sigma(R_d) \left( \frac{M_{*,1} + M_{d,1}}{M_{\text{tot}}} \right) \times \exp \left[ -\frac{2^{5/2}}{3} \left( \frac{M_{*,2}}{M_{\text{tot}}} \right)^{1/2} \left( \frac{r_p}{R_d} \right)^{3/2} \right]$$

is a rapidly decreasing function of the ratio  $r_p/R_d$ . Equation (8) is only valid when  $r_p > R_d$ , which is satisfied by our simulation sets 'PARA3' – 'PARA5', with 'PARA3' being a marginal case, since the two discs overlap near pericenter. Figure 10 shows the fractional change in disc angular momentum (Equation 8 normalized by  $L_{\text{disc}}$ ) evaluated for our disc model with  $M_* = 0.45 M_\odot$ ,  $M_d = 0.05 M_\odot$  and  $R_d = 60.0$  AU. For 'PARA4' and 'PARA5', the victim disc experiences changes in angular momentum that are at the level of 1% and below. Since  $L_{\text{disc}}/|L_{\text{orb}}| \sim 0.03$  and 0.02 for 'PARA4' and 'PARA5' respectively, the angular momentum exchange between the disc and the orbit is of the order of  $10^{-4}$  times smaller than  $|L_{\text{orb}}|$  which is more than an order of magnitude smaller than the change we observe in Figure 9. This suggests that the orbital evolution of 'PARA4' and 'PARA5' is either dominated by accretion, noise or perhaps amplified by the presence of a second disc. On the other hand, 'PARA3' shows a loss in inner angular momentum of 40% for nearly prograde encounters and a negligible gain during retrograde encounters. Since in 'PARA3'  $L_{\text{disc}}/|L_{\text{orb}}| \sim 0.04$ , the victim disc is expected to lose angular momentum to the binary orbit by an amount of the order of 2% of  $|L_{\text{orb}}|$ . Although this is the correct order of magnitude for the change in  $|L_{\text{orb}}|$  observed for 'PARA3' (Figure 9), this

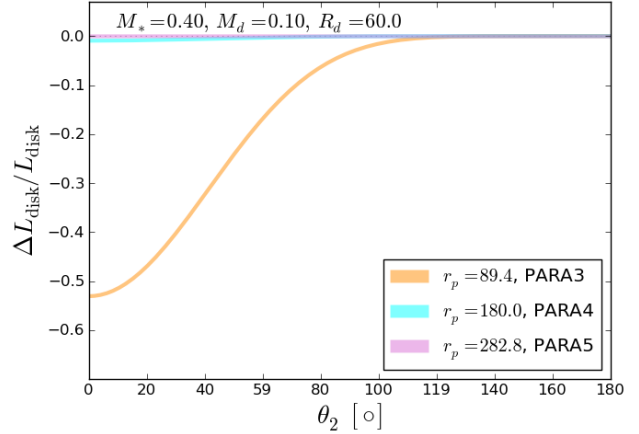


**Figure 10.** Change in a disc's internal angular momentum according to Equation (8) (Ostriker 1994) evaluating the physical and orbital parameters of simulation sets 'PARA3', 'PARA4' and 'PARA5'.

change in orbital angular momentum comes in the form of a *loss* and not a gain. Again, this suggests other mechanisms are at play in addition to tidal forces, and that the simulation set 'PARA3' is outside the regime represented by the work of Ostriker (1994). Interestingly, only 'PARA1' and 'PARA2' show statistically significant gains in angular momentum in some of their examples. However, since at such close encounters the discs collide violently, the departure from the linear regime is too great for sensible interpretation.

According to Equation (8), doubling the mass of the disc while keeping  $M_* + M_d$  constant produces an increase by only  $\sim 20\%$  in  $\Delta L_{\text{disc}}$ , thus requiring very massive discs in order for tidal effects to have a significant impact. We have tested the effect of doubling the disc mass while keeping the sum  $M_* + M_d = 0.5 M_\odot$  constant and run the set of orbits 'PARA4-1' at these higher masses  $M_* = 0.45 M_\odot$  and  $M_d = 0.05 M_\odot$ , and  $M_* = 0.4 M_\odot$  and  $M_d = 0.1 M_\odot$ . Although the more massive discs show hints for richer inner structure, presumably triggered by the lower value of the Toomre  $Q$  parameter, (in this case,  $Q_{\text{T,min}} \approx 2$ ), the orbital evolution seems to be mildly altered by the change in mass. In addition, a simulation with self-gravity artificially turned off is shown for comparison purposes.

Increasing the disc mass dramatically changes the outcome for non-aligned discs. Figure 12 shows the same set-up as Figure 11 but now with the orientations corresponding to 'PARA4-4'. One can see that the stars are rapidly captured after pericenter passage, in striking contrast to the case 'PARA4-1'. In this example, the pericenter separation is larger than twice the disc size (in this case,  $r_p = 180$  AU) and therefore the discs do not collide directly. Because of this, the change in the stars' orbital evolution is not due to radiative losses as in the 'PARA1' cases, but instead due to conservative tidal forces (at least during the early phases of the interaction). As one can expect, the non-axisymmetric tidal features are now more massive in proportion to the discs' increased mass, and therefore can torque the stellar trajectories more effectively. Furthermore, by inclining the discs, the warping modes triggered in the discs make the tidal torque they exert on the stars even stronger (this can already be seen in the linear regime calculations of Ostriker 1994). As opposed to the limit of small disc mass, in which  $L_{\text{tot}} \approx L_{\text{orb}} \sim \text{constant}$ , massive discs with different inclinations

can contribute a significant amount to  $\mathbf{L}_{\text{orb}}$ , making it no longer directed along the  $z$ -direction. For these massive discs, both the disc orientation and the binary orbital plane can be torqued as a result of the encounter. This mutual torquing is strengthened with larger disc mass and with higher mutual inclination, favoring the disruption of the initially parabolic orbits with greater efficiency, even within the short timescales ( $\sim 1$  orbital period) of the simulation.

This work opens interesting possibilities for the outcome of disc-disc interactions well into the non-linear regime. Future work should explore the role of energetics in more detail, studying the interplay between mechanical and thermal energy in the discs, and how realistic cooling prescriptions within the violent compression shocks can affect the results found here.

#### 4 DISCUSSION: ARE DISC ENCOUNTERS LIKELY IN STAR-FORMING REGIONS?

In this work, we have shown that realistic circumstellar discs can affect the orbital evolution of their host stars *provided* the encounters have pericenter separations close to or smaller than the disc sizes. The orbital evolution changes dramatically only for pericenter passages comparable to the disc sizes. Wider encounters may still be important for mis-aligned, massive discs.

Fly-by encounters between young stars at impact parameters of  $\sim 100$  AU (all encounters in our numerical experiments except for the most extreme case ‘PARA1’ for which the impact parameter is set to 50 AU) are likely in dense stellar clusters (see Thies, Kroupa & Theis 2005) provided cluster dispersion does not happen on timescales much shorter than the mean encounter timescale. More generally the cluster lifetime is an important variable since open clusters in the Galactic plane evaporate on timescales of one to a few crossing timescales, or  $\sim 1$  to 3 Myr (Reggiani et al. 2011; Jeffries et al. 2011) with a small fraction reaching up to 10 Myr.

The two-body encounter rate follows a Poisson process if events are not correlated in time. In this case, the probability for one star to suffer at *least* one encounter occurring in any interval of length  $\Delta t$  is  $P_{\Delta t} = 1 - \exp(-\Gamma \Delta t)$ , where the encounter rate  $\Gamma$  is  $\Gamma(b, v) = \pi n b^2 v$  for a given impact parameter and encounter velocity  $v \sim$  the cluster dispersion velocity  $\sigma_v$ . For a spherical cluster, the number density, velocity dispersion and crossing time are respectively:  $n = 3\pi^{1/2} \Sigma_c^{3/2} / (4\bar{m} M_c^{1/2})$ ,  $\sigma_v \approx G^{1/2} (\pi \Sigma_c M_c)^{1/4}$  and  $\tau_{\text{cross}} = M_c^{1/4} G^{-1/2} (\pi \Sigma_c)^{-3/4}$  (e.g., Dukes & Krumholz 2012), where  $\bar{m}$  is the median stellar mass.

For a period of time corresponding to the lifetime of circumstellar discs (say  $\tau_{\text{disc}} \lesssim 10$  Myr), the probability  $P_{\Delta t=\tau_{\text{disc}}}$  can be computed as a function of impact parameter  $b$  for a given cluster mass  $M_c$  and surface density  $\Sigma_c$  (see Thies, Kroupa & Theis 2005, for a similar analysis). For clusters with surface densities of  $\Sigma_c = 1.0 \text{ g cm}^{-2} = 4.7 \times 10^3 \text{ M}_{\odot} \text{ pc}^{-2}$  and masses of  $M_c$  between  $10^{1.5}$  and  $10^{2.5} \text{ M}_{\odot}$  the encounter probability per star can be up to 0.6 for  $b < 100$  AU and  $\approx 1$  at  $b < 400$  AU after 10 Myr. For  $\Sigma_c = 0.1 \text{ g cm}^{-2}$  the encounter probabilities are still high, 0.01 to 0.02 at 100 AU and 0.1 to 0.2 at 400 AU.

Young clusters disperse after gas expulsion, and the number density of objects decreases rapidly after a few crossing times (e.g. Elmegreen 2000; Hartmann, Ballesteros-Paredes & Bergin 2001; Lada & Lada 2003). Since  $\tau_{\text{cross}}$  will almost invariably be shorter than  $\tau_{\text{disc}}$ , the realistic probability of encounter has an upper bound of  $P_{\Delta t=\tau_{\text{cross}}}$ . In this case, the likelihood of an encounter depends only on  $\Sigma_c$  (this was pointed out by Dukes & Krumholz 2012, but see Craig & Krumholz 2013 for a discussion on the validity of this

result). If the waiting time is only one crossing time, the chance of an encounter as a function of  $b$  becomes two orders of magnitude smaller than the previous estimate. For the impact parameters explored in our numerical simulations (50, 100, 200, 300 and 400 AU before gravitational focusing) the probability of a star undergoing such encounters is roughly  $10^{-4}$ ,  $5 \times 10^{-3}$ ,  $10^{-3}$ ,  $5 \times 10^{-2}$  and  $10^{-2}$ , respectively, for the values of  $\Sigma_c$  considered. For a median stellar mass of  $\bar{m} \approx 0.6 \text{ M}_{\odot}$ , the range of cluster masses considered here imply a few tens to a few hundred members. Thus, for the most optimistic cluster properties, we expect a global number of encounters per cluster of order unity. This can be expressed by the number of encounters per star expected within a crossing time. A simple estimate gives

$$N_{\text{enc,exp}} \approx \langle \Gamma(b, v) \rangle \times t_{\text{cross}} = \frac{3}{4} \pi b^2 \frac{\Sigma_c}{\bar{m}}, \quad (9)$$

which is a small number for the cluster parameters explored above.

Thus encounters which dramatically reshape binary orbits are rare, except perhaps for the widest configurations we have considered with (the ‘PARA5’ case). In this case, flybys could still play a role in disc truncation, but owing to tidal forces associated with the central stars rather than ram pressure stripping as is observed in the head-on disc collisions. For the ‘PARA4’ and ‘PARA5’ cases the effect of the finite disc mass on the stellar orbits is negligible, unless the disc masses are increased from  $M_d = 0.11 M_*$  (fiducial case) to, e.g.,  $M_d = 0.25 M_*$ . Including large disc masses is the only way in which discs might play a dynamical role in the evolution of the cluster at small scales due to stellar fly-bys. Since discs in fly-bys should have uncorrelated angular momentum vectors, such encounters would be most similar to the third panel in Figure 12.

Whether such massive discs are realistic is uncertain. Class 0 sources are thought to have up to 85% (Looney, Mundy & Welch 2003) of the mass of the system in the envelope, but it is unclear how much of that mass is in the form of a disc, since both the disc and signatures of Keplerian rotation are difficult to detect due to instrumental and optical depth limitations. Jørgensen et al. (2009) estimated through indirect methods that the submillimeter continuum emission from protostars was consistent with discs having masses as high as  $0.5 \text{ M}_{\odot}$ , however direct evidence of Keplerian rotation was not detected in their Class 0 sample. In contrast, independent modeling (e.g. Chiang et al. 2008) suggests that disc masses in Class 0 objects could be comparable to T Tauri star discs. Of those Class 0 sources for which there is an unambiguous detection of Keplerian rotation, thus far only L1527 has a (model dependent) estimate of a disc mass, which is  $\lesssim 1\%$  of the protostar mass (Chiang, Looney & Tobin 2012; Tobin et al. 2013). But, even in this case, evidence may not be conclusive, as optical-depth effects may underestimate the disc mass, which could be as high as half the host star mass as argued by Forgan & Rice (2013). Such a massive disc would enable angular momentum transport via gravitational instabilities, which in turn would be consistent with the inferred accretion rate of this object. In summary, although disc-to-star mass ratios of 0.25 provide enough torques onto the stellar orbits to produce quick orbital decay, Observational evidence is not yet conclusive as to whether such massive Class 0 discs exist. Future Atacama Large Millimeter Array data will help resolve this question (Segura-Cox et al, in prep).

If very high disc masses are not confirmed, enhancements in the encounter rates owing to realistic cluster substructure might lead to a greater encounter frequency, too. As these fractal clusters undergo relaxation and dispersal, Craig & Krumholz (2013)



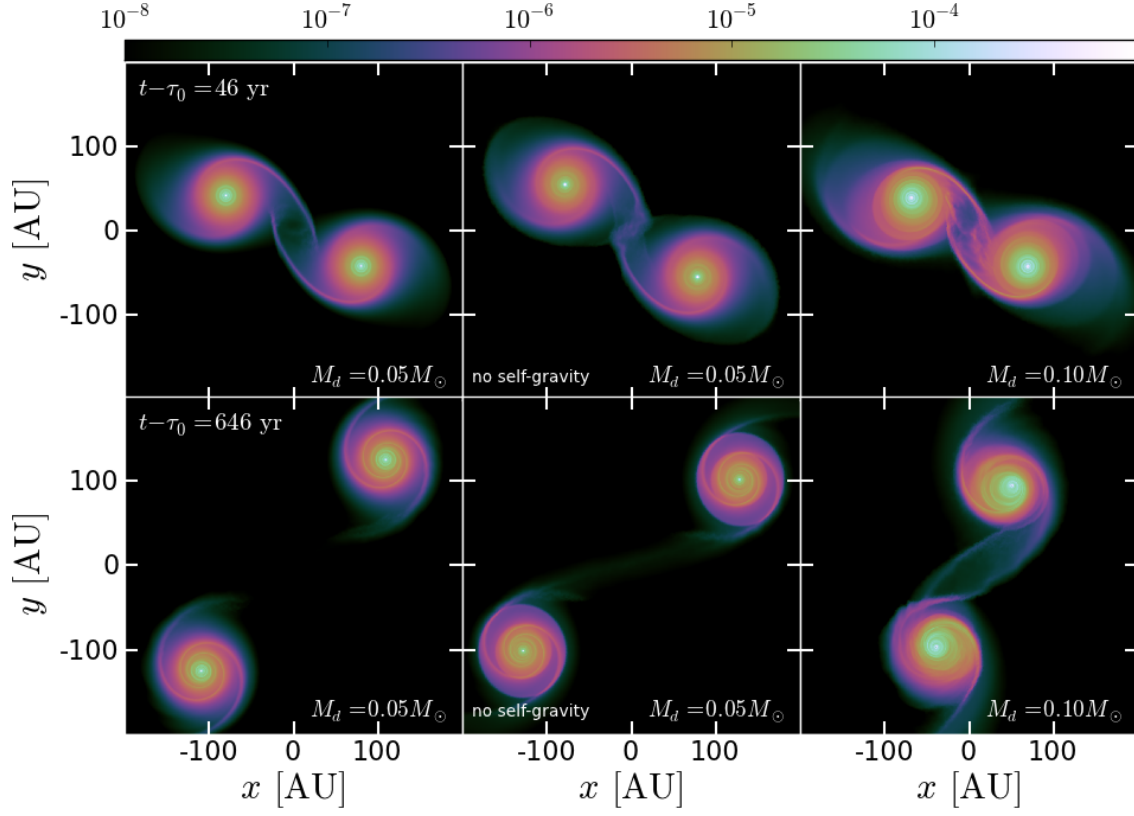


**Figure 11.** Encounter with configuration ‘PARA4-1’ ( $r_p = 180.0$ ,  $\theta_1 = 0$ ,  $\theta_2 = 0$ ) at two different times for three different mass scalings. Left panel: encounter with mass ratio of  $M_d/M_* = 0.05/0.45$  (one of the main simulations listed in Table 1). Middle panel: simulation ‘PARA4-1’ but with self-gravity turned off, i.e., effectively a mass ratio of  $M_d/M_* = 0$ . Right panel: encounter  $M_d/M_* = 0.1/0.4$ .

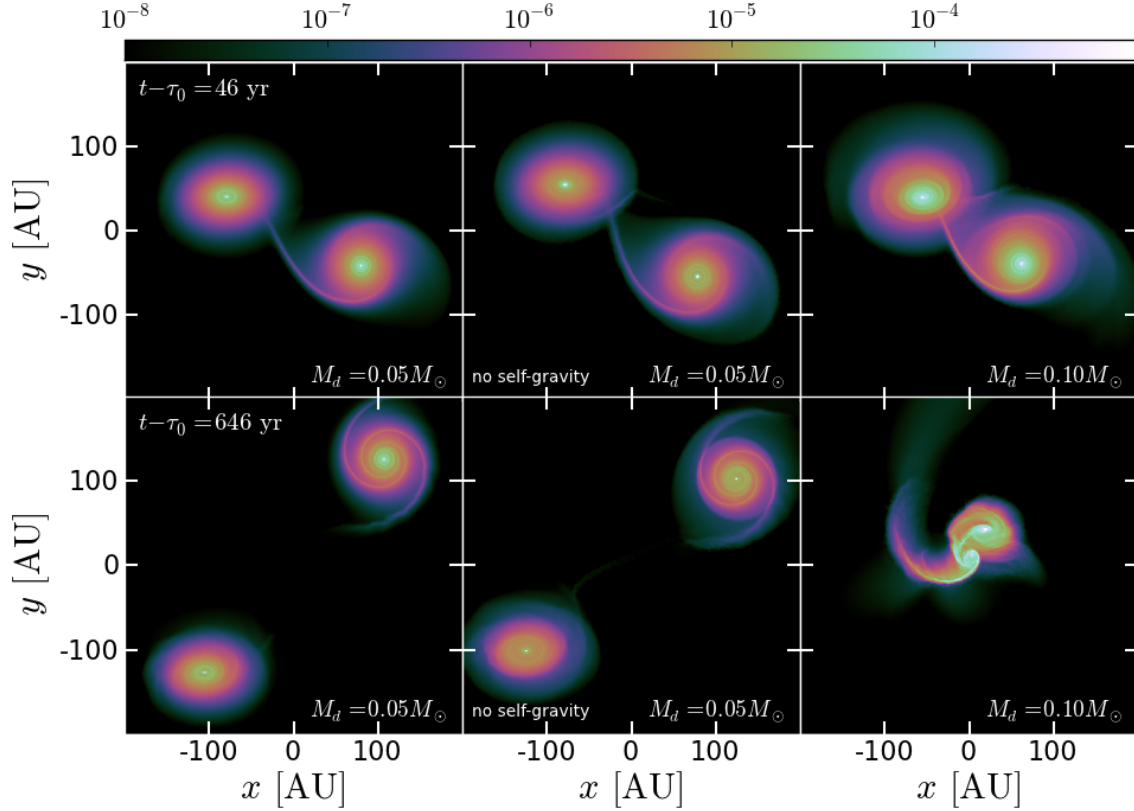


**Figure 12.** Same as Figure 11 but with disc orientations as those of simulation ‘PARA4-4’ ( $r_p = 180.0$ ,  $\theta_1 = 0$ ,  $\theta_2 = 135$ ).



found the number of encounters can be one or two orders of magnitude higher than the relaxed-cluster estimate of Equation (9). In fact, in their numerical experiments Craig & Krumholz (2013) find that  $\gtrsim 50\%$  of the close encounters (defined by those authors as all those within  $b = 1000$  AU) take place within a crossing time, before the rates go down to values consistent with Equation (9). For some of their densest cluster models, these authors find that the number of encounters per star can be in the hundreds. Assuming that the probability distribution of impact parameters is still described by  $p(b)db \propto b db$ , encounters at  $b \sim 500$  AU will be four times less likely than at 1000 AU, and those at  $b \sim 100$  AU will be 100 times less likely, still allowing for a few encounters per star to take place before the cluster disperses. These considerations expand the parameter space available for plausible disc encounters to include most of the impact parameters explored in our numerical experiments.

Although the orbital decay/capture of the stars is still a sensitive function of disc/envelope mass, the increased encounter rates given by Craig & Krumholz (2013) (which are independent of disc mass) imply that flyby disc encounters could provide a means for truncation early on in the disc lifetime. Extreme environments like Orion nebular cluster may already provide the evidence of this process having taken place, as suggested by de Juan Ovelar et al. (2012).

## 5 SUMMARY

We have carried out simulations of binary disc encounters using the moving-mesh code AREPO. We have focused our analysis on the effects of tidal forces on a stellar pair in a parabolic orbit, exploring the outcome of disc-disc interactions well into the non-linear regime.

We have found that the orbital energy and orbital angular momentum change per passage depend sensitively on the separation at pericenter. This result is qualitatively consistent with tidal torque calculations of star-disc interactions for parabolic and hyperbolic orbits (Ostriker 1994). One surprising result, however, is the outcome of “runaway orbital decay” in those simulations with small pericenter separations ( $r_p \sim R_{\text{disc}}$ ), which show orbital capture with subsequent energy losses at each pericenter encounter, hastening disc dispersal and eventually forming close binaries with diffuse circumbinary discs. This process is particularly fast for retrograde discs. We expect this result to be very sensitive to the gas equation of state, and thus future work should explore the role of cooling prescriptions or realistic radiative transfer on the dynamics of discs affected by violent compression shocks.

The applicability of our numerical results to real astrophysical systems remains to be assessed by upcoming high resolution observations of circumstellar discs. In principle, the configurations explored here may be too extreme to be common. Indeed, in most nearby Galactic star forming regions, the effective surface density of protostellar clusters is too low to produce more than  $\sim 10^{-3}$  encounters *per star* before the clusters dissipates (a timescale typically shorter than the lifetime of discs). However, there is some evidence of strongly interacting circumstellar discs with morphologies that could in principle be explained by stellar flybys (see Cabrit et al. 2006; Salyk et al. 2014). In the near future, ALMA continuum and line data will provide a large sample of discs in binaries which will help to address the statistical relevance of those existing candidates and measure the frequency of flyby disc pairs. If flybys are found to be more frequent than expected from the simple arguments

above, cluster substructure is a plausible explanation for enhanced rates (Craig & Krumholz 2013). There is clear evidence that young clusters are not uniform, spherical, virialized systems, but instead have significant fractal-like substructure (in both gas and stars; see e.g., Elmegreen 2000; Lada & Lada 2003; Cartwright & Whitworth 2004; Gutermuth et al. 2011).

Similarly, new data on circumbinary gas discs from ongoing and future surveys will test different formation mechanisms for such systems. The occurrence rate of circumbinary discs will help provide answers to the question of whether these form in an analogous manner to discs around single stars, or if their frequency is modulated by other “non-primordial” formation mechanisms such as the ones produced by the simulations in this work.

Our experiments of isolated disc encounters allow for a detailed analysis of disc evolution in densely packed star forming regions, where disc truncation can take place, in contrast to global cluster simulations, for which an accurate description of the disc dynamics may be too costly or impossible to implement (e.g. Bate 2012; Rosotti et al. 2014). The exploration of the role of cluster kinematics on disc evolution via isolated flybys may help provide a link between the environmental properties of the parent cluster and the planet forming capabilities of a young star. Under this scenario, the planet forming efficiency will not only depend on the mass, metallicity and dust content of a star and its surrounding disc, but also on the location within the birth cluster and on the overall properties of the latter.

## ACKNOWLEDGEMENTS

The research presented here was largely carried out as part of DJM’s PhD thesis at Harvard University. The simulations in this paper were run on the Odyssey cluster supported by the FAS Science Division Research Computing Group at Harvard University. DJM would like to thank Dimitar Sasselov, Matthew Holman, Ruth Murray-Clay and James Stone for insightful feedback and support throughout the development of this work. DJM acknowledges partial support from the Fulbright-CONICYT graduate fellowship program.

## REFERENCES

- Adams F. C., Laughlin G., 2001, *Icarus*, 150, 151
- Adams F. C., Proszkow E. M., Fatuzzo M., Myers P. C., 2006, *ApJ*, 641, 504
- Alexander R., 2012, *ApJ*, 757, L29
- Anderson K. R., Adams F. C., Calvet N., 2013, *ApJ*, 774, 9
- Andrews S. M., Williams J. P., 2007, *ApJ*, 659, 705
- Andrews S. M., Wilner D. J., Hughes A. M., Qi C., Dullemond C. P., 2009, *ApJ*, 700, 1502
- Artymowicz P., Lubow S. H., 1994, *ApJ*, 421, 651
- Barnes J., Hut P., 1986, *Nature*, 324, 446
- Barth T. J., 1992, in *AGARD, Special Course on Unstructured Grid Methods for Advection Dominated Flows*. ed. C. Johnson. Specialised Printing Services Limited. Loughton, England
- Bate M. R., 2011, *MNRAS*, 417, 2036
- Bate M. R., 2012, *MNRAS*, 419, 3115
- Bauer A., Springel V., 2012, *MNRAS*, 423, 2558
- Binney J., Tremaine S., 2008, *Galactic Dynamics: Second Edition*. Princeton University Press

- Boffin H. M. J., Watkins S. J., Bhattal A. S., Francis N., Whitworth A. P., 1998, *MNRAS*, 300, 1189
- Cabrit S., Pety J., Pesenti N., Dougados C., 2006, *A & A*, 452, 897
- Cartwright A., Whitworth A. P., 2004, *MNRAS*, 348, 589
- Chen X. et al., 2013, *ApJ*, 768, 110
- Chiang H.-F., Looney L. W., Tassis K., Mundy L. G., Mouschovias T. C., 2008, *ApJ*, 680, 474
- Chiang H.-F., Looney L. W., Tobin J. J., 2012, *ApJ*, 756, 168
- Clarke C. J., Pringle J. E., 1991a, *MNRAS*, 249, 584
- Clarke C. J., Pringle J. E., 1991b, *MNRAS*, 249, 588
- Craig J., Krumholz M. R., 2013, *ApJ*, 769, 150
- Davis M., Efstathiou G., Frenk C. S., White S. D. M., 1985, *ApJ*, 292, 371
- de Juan Ovelar M., Kruijssen J. M. D., Bressert E., Testi L., Bastian N., Cánovas H., 2012, *A & A*, 546, L1
- Dehnen W., Aly H., 2012, *MNRAS*, 425, 1068
- D’Onghia E., Vogelsberger M., Faucher-Giguere C.-A., Hernquist L., 2010, *ApJ*, 725, 353
- Dukes D., Krumholz M. R., 2012, *ApJ*, 754, 56
- Elmegreen B. G., 2000, *ApJ*, 530, 277
- Forgan D., Rice K., 2009, *MNRAS*, 400, 2022
- Forgan D., Rice K., 2013, *MNRAS*, 433, 1796
- Gingold R. A., Monaghan J. J., 1977, *MNRAS*, 181, 375
- Gradshteyn I. S., Ryzhik, 2000, *Table of Integrals, Series, and Products*. Academic Press
- Gutermuth R. A., Pipher J. L., Megeath S. T., Myers P. C., Allen L. E., Allen T. S., 2011, *ApJ*, 739, 84
- Hale A., 1994, *AJ*, 107, 306
- Harris R. J., Andrews S. M., Wilner D. J., Kraus A. L., 2012, *ApJ*, 751, 115
- Hartmann L., Ballesteros-Paredes J., Bergin E. A., 2001, *ApJ*, 562, 852
- Hernquist L., Katz N., 1989, *ApJS*, 70, 419
- Jeffries R. D., Littlefair S. P., Naylor T., Mayne N. J., 2011, *MNRAS*, 418, 1948
- Jørgensen J. K., van Dishoeck E. F., Visser R., Bourke T. L., Wilner D. J., Lommen D., Hogerheijde M. R., Myers P. C., 2009, *A & A*, 507, 861
- Kratter K. M., Matzner C. D., Krumholz M. R., 2008, *ApJ*, 681, 375
- Kratter K. M., Murray-Clay R. A., Youdin A. N., 2010, *ApJ*, 710, 1375
- Kraus A. L., Ireland M. J., 2012, *ApJ*, 745, 5
- Lada C. J., Lada E. A., 2003, *ARA&A*, 41, 57
- Larwood J. D., Nelson R. P., Papaloizou J. C. B., Terquem C., 1996, *MNRAS*, 282, 597
- Ledoux P., 1951, *Annales d’Astrophysique*, 14, 438
- Lin D. N. C., Laughlin G., Bodenheimer P., Rozyczka M., 1998, *Science*, 281, 2025
- Looney L. W., Mundy L. G., Welch W. J., 2003, *ApJ*, 592, 255
- Lucy L. B., 1977, *AJ*, 82, 1013
- Lynden-Bell D., Pringle J. E., 1974, *MNRAS*, 168, 603
- Mestel L., 1963, *MNRAS*, 126, 553
- Mocz P., Vogelsberger M., Hernquist L., 2014, *MNRAS*, 442, 43
- Mocz P., Vogelsberger M., Sijacki D., Pakmor R., Hernquist L., 2014, *MNRAS*, 437, 397
- Moeckel N., Bally J., 2006, *ApJ*, 653, 437
- Monaghan J. J., 1992, *ARA&A*, 30, 543
- Muñoz D. J., Kratter K., Springel V., Hernquist L., 2014, *MNRAS*, 445, 3475
- Muñoz D. J., Springel V., Marcus R., Vogelsberger M., Hernquist L., 2013, *MNRAS*, 428, 254
- Murillo N. M., Lai S.-P., Bruderer S., Harsono D., van Dishoeck E. F., 2013, *A & A*, 560, A103
- Ogilvie G. I., Dubus G., 2001, *MNRAS*, 320, 485
- Ostriker E. C., 1994, *ApJ*, 424, 292
- Pakmor R., Bauer A., Springel V., 2011, *MNRAS*, 418, 1392
- Pakmor R., Springel V., 2013, *MNRAS*, 432, 176
- Parker R. J., Quanz S. P., 2012, *MNRAS*, 419, 2448
- Petkova M., Springel V., 2011, *MNRAS*, 415, 3731
- Pfalzner S., 2003, *ApJ*, 592, 986
- Pfalzner S., Olczak C., 2007, *A & A*, 462, 193
- Pfalzner S., Umbreit S., Henning T., 2005, *ApJ*, 629, 526
- Picogna G., Marzari F., 2014, *A & A*, 564, A28
- Reggiani M., Robberto M., Da Rio N., Meyer M. R., Soderblom D. R., Ricci L., 2011, *A & A*, 534, A83
- Rosotti G. P., Dale J. E., de Juan Ovelar M., Hubber D. A., Kruijssen J. M. D., Ercolano B., Walch S., 2014, *MNRAS*, 441, 2094
- Sales L. V., Marinacci F., Springel V., Petkova M., 2014, *MNRAS*, 439, 2990
- Salyk C., Pontoppidan K., Corder S., Muñoz D., Zhang K., Blake G. A., 2014, *ApJ*, 792, 68
- Shen S., Wadsley J., Hayfield T., Ellens N., 2010, *MNRAS*, 401, 727
- Sheppard S. S., Trujillo C. A., 2006, *Science*, 313, 511
- Sijacki D., Vogelsberger M., Kereš D., Springel V., Hernquist L., 2012, *MNRAS*, 424, 2999
- Springel V., 2010a, *MNRAS*, 401, 791
- Springel V., 2010b, *ARA&A*, 48, 391
- Springel V., 2011, in *Tessellations in the Sciences: Virtues, Techniques and Applications of Geometric Tilings*, eds. R. van de Weijgaert, G. Vegter, J. Ritzerveld and V. Icke, (arxiv:1109.2218)
- Springel V., Di Matteo T., Hernquist L., 2005, *MNRAS*, 361, 776
- Springel V., Yoshida N., White S. D. M., 2001, *New Astron.*, 6, 79
- Thies I., Kroupa P., Goodwin S. P., Stamatellos D., Whitworth A. P., 2010, *ApJ*, 717, 577
- Thies I., Kroupa P., Theis C., 2005, *MNRAS*, 364, 961
- Tobin J. J., Hartmann L., Chiang H.-F., Wilner D. J., Looney L. W., Loinard L., Calvet N., D’Alessio P., 2013, *ApJ*, 771, 48
- Toomre A., Toomre J., 1972, *ApJ*, 178, 623
- Toro E. F., 2009, *Riemann solvers and numerical methods for fluid dynamics. A practical introduction*. 3rd Edition. Springer
- Vogelsberger M., Genel S., Sijacki D., Torrey P., Springel V., Hernquist L., 2013, *MNRAS*, 436, 3031
- Vogelsberger M., Sijacki D., Kereš D., Springel V., Hernquist L., 2012, *MNRAS*, 425, 3024
- Wang H.-H., Klessen R. S., Dullemond C. P., van den Bosch F. C., Fuchs B., 2010, *MNRAS*, 407, 705
- Watkins S. J., Bhattal A. S., Boffin H. M. J., Francis N., Whitworth A. P., 1998a, *MNRAS*, 300, 1205
- Watkins S. J., Bhattal A. S., Boffin H. M. J., Francis N., Whitworth A. P., 1998b, *MNRAS*, 300, 1214

## APPENDIX A: ISOLATED THIN DISC MODELS

### A1 Model characteristics and initial conditions

To obtain stable initial disc conditions we enforce radial centrifugal and vertical hydrostatic equilibrium:

$$-\frac{v_\phi^2}{R} = -\frac{1}{\rho} \frac{\partial p}{\partial R} - \frac{\partial \Phi_0}{\partial R} - \frac{\partial \Phi_g}{\partial R}, \quad (\text{A1})$$

$$0 = -\frac{1}{\rho} \frac{\partial p}{\partial z} - \frac{\partial \Phi_0}{\partial z} - \frac{\partial \Phi_g}{\partial z}, \quad (\text{A2})$$

where  $\Phi_0(R, z)$  is the potential due to the central star and  $\Phi_g(R, z)$  is the potential due to gas self-gravity. Equation (A1) determines the azimuthal velocity field  $v_\phi^2(R, z)$  while Equation (A2) contains the solution for the vertical structure of the disc at all radii.

The models used here are based on the Lynden-Bell-Pringle surface density profile (Lynden-Bell & Pringle 1974; Equation 3). We use a fixed temperature profile of the form  $T(R) = T_c (R/R_c)^{-l}$  with power-law index fixed to  $l = 0.5$ . The disc characteristic radius is set to  $R_c = 20$  AU and the total mass of the system (star plus disc) to  $0.5 M_\odot$ . The disc-to-star mass ratio is varied from  $M_d/M_* = 0.02$  up to  $0.67$ , always keeping  $M_* + M_d = 0.5 M_\odot$ . The normalization of the temperature profile is chosen according to a specified aspect ratio at  $R_c$ , producing a flared disc with aspect ratio

$$h(R) \equiv \frac{c_s(R)}{v_K(R)} = \sqrt{\frac{k_B T(R)}{\mu m_H} \frac{R}{GM_*}} \equiv h_c \left( \frac{R}{R_c} \right)^{-(l-1)/2}. \quad (\text{A3})$$

We vary  $h_c$  from  $0.04$ – $0.1$ . The minimum value of  $h_c$  is set by resolution constraints: for smaller values a proper three-dimensional description requires  $N_{\text{gas}} \sim 10^7$ .

All singular terms in Equations (3) and (A3) are regularized using a spline softening with softening parameter  $s$  akin to that used for the gravitational potential of the central stars and of individual gas cells (Hernquist & Katz 1989; Springel, Yoshida & White 2001). In this case, the central gravitational potential  $\Phi_0$  reaches a finite value at  $R = 0$  (the position of the star) and recovers its exact Keplerian value at  $R = 2.8s$ . This means that the Keplerian angular speed  $\Omega_K^2 = (\partial \Phi_0 / \partial R) / R$  vanishes at  $R = 0$ .

### A2 Mesh generation and vertical structure

We tessellate the domain using a *mass resolution* criterion, in which the domain is discretized by a Monte-Carlo sampling of an underlying density field. Given a number of mesh-generating points  $N_{\text{gas}}$ , a gas disc of total mass  $M_d$  is split into cells of nearly equal mass  $m_{\text{gas}} = M_d / N_{\text{gas}}$ . We assume a 3-D density field of the form  $\rho(R, z) = \Sigma(R) \zeta(R, z)$ , where  $\int_{-\infty}^{+\infty} \zeta(R, z) dz = 1$ . Because the density field is not separable into  $R$  and  $z$  components, we sample the radial positions  $\{R_i\}$  first and then sample the vertical positions  $\{z_i\}_R$  for fixed  $R$ <sup>3</sup>. The azimuthal coordinate  $\phi$  is drawn from a uniform distribution in  $[0, 2\pi)$ .

The vertical profile at a given  $R$ ,  $\zeta(z|R)$  must be obtained numerically for self-gravitating discs. We have adapted the potential method described in detail in Wang et al. (2010) (see also Springel, Di Matteo & Hernquist 2005). This technique consists of iterating between vertical hydrostatic equilibrium equation – under a fixed

vertical potential – and the vertical Poisson equation – for a given vertical density profile – until convergence is achieved. The geometrically thin disc approximation allows us to solve for two coupled ordinary differential equations instead of a set of partial differential equations. We force the separability of the potential of a very flattened system into a mid-plane component and a local vertical component in the form  $\Phi_g(R, z) = \Phi_g(R, 0) + \Phi_{g,z}(R, z)$  (Binney & Tremaine 2008), such that a local, 1-D Poisson equation can be written in the variable  $z$  for fixed  $R$ . We use a locally isothermal equation of state, in which the sound speed only depends on the radial coordinate  $R$ , such that  $p = c_s^2(R)\rho$ . This approximation, combined with Equation (A2) and provided we know the mid-plane density  $\rho(R, 0) \equiv \rho_0(R)$  allows us to solve for the vertical density profile:

$$\rho(R, z) = \rho_0(R) \exp \left( -\frac{\Phi_{0,z} + \Phi_{g,z}}{c_s^2(R)} \right). \quad (\text{A4})$$

where  $\Phi_{0,z} \equiv \Phi_0(R, z) - \Phi_0(0, z)$  is the  $z$ -dependent part of the Keplerian potential  $\Phi_0$  of the central star

Starting with an initial guess for the midplane density  $\rho_0^{(0)}(R)$  and for disc self-potential  $\Phi_{g,z}^{(0)} = 0$ , Equation (A4) can be used to solve to obtain a full density profile from which a new potential can be derived, which in turns allows for a new estimate of the midplane density. The iteration steps are (for fixed  $R$ ):

$$\text{(I)} \quad \rho_0^{(k+1)} = \frac{\Sigma(R)}{\int_{-\infty}^{\infty} \rho^{(k)}(z) dz} \quad (\text{A5a})$$

$$\text{(II)} \quad \text{solve numerically for } \Phi_{g,z}^{(k+1)} \\ \frac{d}{dz} \left( \frac{\Phi_{g,z}^{(k+1)'}}{\Phi_{g,z}^{(k+1)}} \right) = \left( \frac{4\pi G \rho^{(k)}(z)}{\Phi_{g,z}^{(k+1)'}} \right) \quad (\text{A5b})$$

$$\text{(III)} \quad \rho^{(k+1)}(z) = \rho_0^{(k+1)} \exp \left( -\frac{\Phi_{0,z} + \Phi_{g,z}^{(k+1)}}{c_s^2} \right). \quad (\text{A5c})$$

For low mass circumstellar discs ( $M_d \lesssim 0.05 M_*$ ) convergence can be achieved within at most 5-6 iterations using as the initial guess a Gaussian-profile disc. If discs are massive ( $M_d \gtrsim 0.1 M_*$ ), convergence is achieved most quickly using the self-gravitating slab (Ledoux 1951) as the initial guess (even though it neglects the presence of the star's Keplerian potential). For discs masses of  $M_d \sim 0.2 M_*$ , the latter approach needs at most  $\sim 9$  iterations for convergence.

For the number of mesh-generating points per disc that are used in the study, the evaluation of the density field is complete in the vertical direction up to  $\sim 3$  scale-heights. Beyond this point, the mesh transitions into a quasi-regularly spaced mesh that connects to the coarse background cells that fill the computational domain (see Springel 2010a for a detailed description).

To minimize the Poisson noise of the sampling, we take advantage of the Eulerian nature of AREPO and impose the exact value of the density field at the mesh-generating points, instead of forcing an homogeneous cell mass  $m_{\text{gas}}$  throughout the disc. This additional step – only possible with AREPO – produces very smooth density fields, at the expense of a variation in cell mass, although this can be mitigated. Figure A1 shows the distribution of cell masses as generated by the initial condition algorithm (top panel) and how the spread in cell masses can be corrected (bottom panel) by a series of refinement and derefinement steps (Springel 2010a). Figure A1 also shows the distribution of “background cells”, which are very

<sup>3</sup> The 1-D function  $\Sigma(R)$  is sampled through conventional methods to produce a set  $\{R_i\}$  of size  $N_{\text{gas}}$ . Assuming the variability in  $R$  is slower than that in  $z$ , the  $\{R_i\}$  are grouped into radial bins and proceed to Monte-Carlo sample the 1-D function  $\zeta(z|R)$  to obtain values for the  $z$ -coordinate.

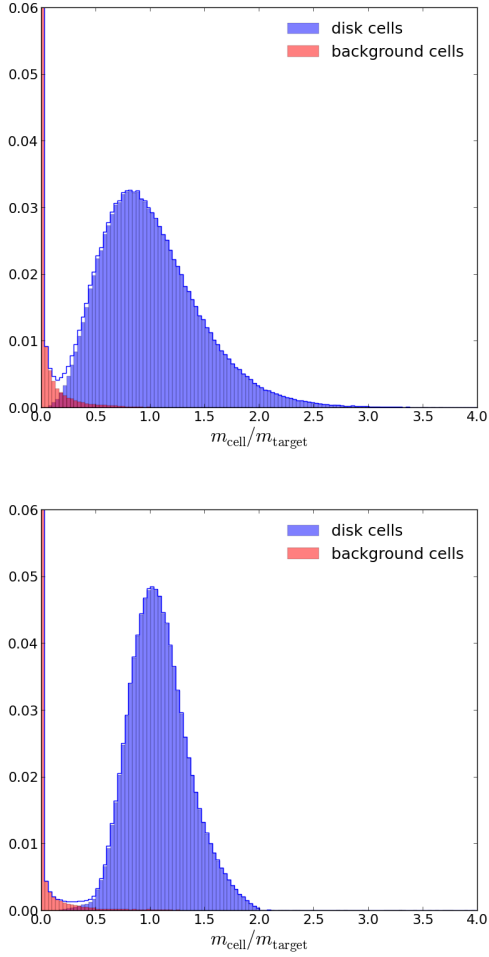


**Figure A1.** Mass distribution of Voronoi cells resulting from the tessellation of Monte-Carlo sampled points (top panel) and the distribution resulting from refinement/derefinement of cells above/below the mass limit 0.5/2.0 times the reference mass  $m_{\text{target}}$  (bottom panel).

low mass cells or large volume that fill in the computational box. Ideally, these two cell distributions should smoothly transition into one another (see Figure 1).

We confirm that the prescribed surface density  $\Sigma(R)$  is recovered from the 3D models by integrating the density field along the vertical direction.

### A3 Velocity structure

The velocity field of a stationary, axisymmetric system is given by the solution for  $v_\phi$  in Equation (A1). The velocity is not exactly Keplerian due to the negative contribution of the pressure gradient and disc self-gravity. In addition, three-dimensional discs will have a small vertical gradient in orbital speed which causes the upper layers to rotate more slowly than the mid-plane. Qualitatively,

$$v_\phi^2 = (\text{Keplerian term})^2 + (\text{self-gravity term})^2 + (\text{pressure term})^2 + (\text{vertical layering term})^2. \quad (\text{A6})$$

For discs with masses greater than  $0.02 M_*$ , the self-gravity term is comparable to, or greater than the pressure term, although it only starts to cause a significant deviation from Keplerian rotation for  $M_d/M_* \gtrsim 0.3$ .

The velocity field in three dimensions, for locally isothermal

discs, is (see Wang et al. 2010)

$$\frac{v_\phi^2}{R} = \frac{v_c^2}{R} - \frac{1}{\rho} \frac{\partial p}{\partial R} \Big|_{z=0} - \frac{\partial c_s^2}{\partial R} \ln \left( \frac{\rho(R, z)}{\rho_0(R)} \right), \quad (\text{A7})$$

where  $v_c^2 = v_K^2(z=0) + v_{c,d}^2$  is the circular speed due to gravity (from both the central star and the disc). Thus the vertically-layered rotation curve can be obtained by first calculating the two-dimensional rotation curve corresponding to a highly-flattened disc (Binney & Tremaine 2008) and then adding a correction due to the vertical structure (Wang et al. 2010).

The component of the circular speed from self-gravity has many possible functional forms (see Binney & Tremaine 2008). For numerical computations, we have found that a formula due to Mestel (1963) is particularly useful:

$$v_{c,d}^2(R) = G \frac{M_d(< R)}{R} + 2G \sum_{k=1}^{\infty} \alpha_k \left[ \frac{(2k+1)}{R^{2k+1}} \int_0^R dR' \Sigma(R') R'^{2k+1} - 2k R^{2k} \int_R^{\infty} dR' \frac{\Sigma(R')}{R'^{2k}} \right] \quad (\text{A8})$$

Although the summation in Equation (A8) does not converge rapidly, it is a convenient representation of  $v_{c,d}^2$  for numerical computation, since it involves only well-behaved integrals and simple sums. If a tolerance parameter magnitude of  $10^{-6}$  is introduced relative to the zeroth order term ( $GM_d(< R)/R$ ), only the first  $\sim 10$  terms in the sum are necessary. In pathological cases where more terms are required, the sum is extended to  $\sim 20$ . This typically happens for small  $R$ , where often times the inaccuracy in  $v_{c,d}^2$  is negligible relative to the dominant Keplerian term  $v_K^2$ .

For a density profile index of  $p = 1$ , the self-gravity contribution to the disc's rotation curve can be calculated exactly (see Appendix B). Although the analytic solution to  $v_{c,d}^2(R)$  is too complicated to be useful in practice (it involves Meijer functions), it can be used for debugging purposes and to compare to the numerical output of the truncated series in Equation (A7). This solution can be written

$$v_{c,d}^2(R) = \frac{GM_d}{R_c} f\left(\frac{R}{R_c}\right), \quad (\text{A9})$$

where  $f(x)$  is a dimensionless function<sup>4</sup> of order unity which involve Meijer-G functions (Appendix B) and that equals 1 at  $R = 0$  and approaches  $R_c/R$  as  $R \rightarrow \infty$  (i.e. the disc potential approaches a Keplerian form at large distances).

However, since  $\Sigma(R)$  in Equation (3) diverges at the origin, the surface density there is infinite. The derivative of the gravitational field due to this mass distribution (Binney & Tremaine 2008, Eq. 2.188) takes a finite value of  $GM_d/R_c$  at the origin, which is an unphysical value for the circular speed. Any continuous distribution of matter should have a vanishing circular speed at the origin, and this can be obtained by smoothing out the singular term in  $\Sigma(R)$  as explained above. This produces a circular speed profile that is zero at the origin, but rapidly converges to the exact profile

<sup>4</sup> The functional form of this dimensionless function is

$$f(x) = \frac{x}{2\sqrt{\pi}} G_{13}^{21} \left( \frac{x^2}{4} \middle| -\frac{1}{2}, \frac{1}{2}, -\frac{1}{2} \right). \quad (\text{A10})$$

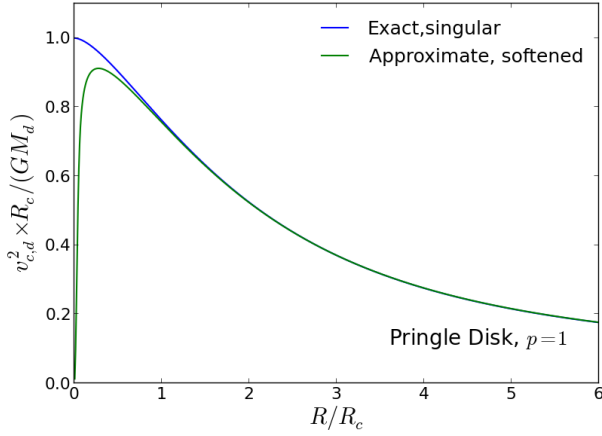


**Figure A2.** Circular speed profile of a Lynden-Bell-Pringle disc owing to its own self-gravity. The blue line depicts the exact computation of  $v_{c,d}^2$  (Equation A9) for the singular profile  $\Sigma(R)$  of Equation (3) for a power-law index  $p = 1$  normalized by  $GM_d/R_c$ . The green line shows the self-gravity contribution to  $v_\phi$  we actually use in our models (calculated through a truncated version of Equation (A8) by numerical integration using a version of  $\Sigma(R)$  softened at the origin.

far from  $R = 0$ . This is shown in Figure A2, where the numerically obtained form of the circular speed (Equation (A8)) changes continuously from zero to the profile given by Equation (A9).

## APPENDIX B: EXACT ROTATION CURVE FOR A MASSIVE LYNDEN-BELL-PRINGLE DISC WITH $p = 1$

In the special case of  $p = 1$ , the Lynden-Bell-Pringle surface density profile takes the form

$$\Sigma(R) = \frac{M_d}{2\pi R_c^2} \left( \frac{R}{R_c} \right)^{-1} \exp \left[ -\frac{R}{R_c} \right]. \quad (\text{B1})$$

The circular speed of a disc with this surface density profile can be written in terms of Bessel functions (Binney & Tremaine 2008)

$$v_{c,d}^2(R) = 2\pi GR \int_0^\infty dk k J_1(kR) \int_0^\infty dR' R' \Sigma(R') J_0(kR'). \quad (\text{B2})$$

With  $p = 1$ , the innermost integral in Equation (B2) can be computed with the aid of the identity

$$\int_0^\infty e^{-\alpha x} J_\nu(\beta x) dx = \frac{\beta^{-\nu} [\sqrt{\alpha^2 + \beta^2} - \alpha]^\nu}{\sqrt{\alpha^2 + \beta^2}}$$

(Gradshteyn & Ryzhik 2000, §6.611), with  $\alpha = 1/R_c$ ,  $\beta = k$  and  $\nu = 0$ . This leaves

$$v_{c,d}^2(R) = GM_d \frac{R}{R_c} \int_0^\infty dk k \frac{J_1(kR)}{\sqrt{R_c^{-2} + k^2}}.$$

which can be computed easily if we reformulate the integrand in terms of Meijer-G functions. Using

$$J_\nu(\gamma x) = G_{02}^{10} \left( \frac{\gamma^2 x^2}{4} \middle| \begin{matrix} \frac{1}{2}\nu, & -\frac{1}{2}\nu \end{matrix} \right)$$

(Gradshteyn & Ryzhik 2000, §9.34), and

$$\begin{aligned} \int_0^\infty x^{\rho-1} (x+\beta)^{-\sigma} G_{pq}^{mn} \left( \alpha x \middle| \begin{matrix} a_1, \dots, a_p \\ b_1, \dots, b_p \end{matrix} \right) dx \\ = \frac{\beta^{\rho-\sigma}}{\Gamma(\sigma)} G_{p+1,q+1}^{m+1,n+1} \left( \alpha \beta \middle| \begin{matrix} 1-\rho, a_1, \dots, a_p \\ \sigma-\rho, b_1, \dots, b_p \end{matrix} \right) \end{aligned}$$

(Gradshteyn & Ryzhik 2000, §7.811), we obtain

$$v_{c,d}^2(R) = \frac{GM_d R}{2\sqrt{\pi} R_c^2} G_{13}^{21} \left( \frac{R^2}{4R_c^2} \middle| \begin{matrix} 0 \\ -\frac{1}{2}, \frac{1}{2}, -\frac{1}{2} \end{matrix} \right). \quad (\text{B3})$$

Note that

$$v_{c,d}^2(R) \xrightarrow{R \rightarrow 0} \frac{GM_d}{R_c},$$

i.e., the rotation curve has a non-zero value at the origin. This is due to the divergent surface density at  $R = 0$  in Equation (B1), therefore, a softened surface density profile is needed to reproduce a physically plausible self-gravitating rotation curve that increases from zero at the origin. This explains why the surface density softening cannot be independent from the gravitational softening of the central star, since it must be guaranteed that near  $R = 0$  the rotation curve of the disc is entirely dominated by the point mass.